Available online at www.sciencedirect.com

ScienceDirect

Advances in Space Research 77 (2026) 9764–9783

ADVANCES IN SPACE RESEARCH (a COSPAR publication)

www.elsevier.com/locate/asr

Ground level enhancement GLE #77 on 11 November 2025: a data summary

A.L. Mishev [a], B. Heber [b], K.-L. Klein [c,j], R. Vainio [d], H. Mavromichalaki [e], O. Raukunen [f], N. Larsen [g], N. Petrov [h], N. Nikonov [i], S. Masson [k,j], M. Pesce-Rollins [l], B.T. Kress [m], V. Bindi [i], M. Gerontidou [e], M. Hörlöck [b], S. Koldobskiy [a], E. Riihonen [d], J.V. Rodriguez [m], I. Usoskin [a,n,*]

[a] University of Oulu, Sodankylä Geophysical Observatory and Space Physics and Astronomy Research Unit, Oulu 90014, Finland
[b] Christian-Albrechts-Universitat zu Kiel, Leibnizstr. 11, Kiel24118, Germany
[c] LIRA, Observatoire de Paris, Univ. PSL, Sorbonne Univ., Univ. Paris Cité, CY Cergy Paris Univ., CNRS, 5 Place Jules Janssen, Meudon F-92190, France
[d] University of Turku, Department of Physics and Astronomy, Turku 20014, Finland
[e] National and Kapodistrian University of Athens, Physics Faculty, Zografos 15784, Greece
[f] Aboa Space Research Oy (ASRO), Lemminkäisenkatu 46, Turku 20520, Finland
[g] Nagoya University, Institute for Space-Earth Environmental Research, Nagoya 464-8601, Japan
[h] Institute of Astronomy and National Astronomical Observatory, Bulgarian Academy of Sciences, Tsarigradsko Shose 72, Sofia, BG 1784, Bulgaria
[i] University of Hawaii at Manoa, Physics and Astronomy Department, 2505 Correa Road, Honolulu, HI 96822, USA
[j] Observatoire radioastronomique de Nancay, Observatoire de Paris, Univ. PSL, CNRS, Univ. Orleans, Nancay F 18330, France
[k] Sorbonne Universite, Ecole polytechnique, Institut Polytechnique de Paris, Université Saclay, Observatoire de Paris, Université PSL, CNRS, Laboratoire de Physique des Plasmas (LPP), Paris, France
[l] Istituto Nazionale di Fisica Nucleare, Sezione di Pisa, Pisa I-56127, Italy
[m] Cooperative Institute for Research in Environmental Sciences, University of Colorado Boulder, 216 UCB, Boulder, CO, 80309, USA
[n] Institute for Space-Earth Environmental Research, Nagoya University, Furo-cho, Chikusa-ku, Nagoya 464-8601, Japan

Received 26 December 2025; received in revised form 4 March 2026; accepted 6 March 2026
Available online 12 March 2026

Abstract

A very strong solar energetic particle event took place on 11-Nov-2025. It was registered by the worldwide network of neutron monitors as a ground-level enhancement (GLE) #77, which appeared to be one of the strongest registered GLEs. The peak and integral intensities of GLE #77 reached about 125 (165) % and 600 (800) %·hr, respectively, for standard (bare) neutron monitors. It had a complicated, multi-component anisotropic structure caused by the complexity of the solar coronal and heliospheric conditions. In this work, verified datasets related to this event are provided along with general analyses. The solar and heliospheric conditions are overviewed, including the analysis of solar radio-emission and the location of the primary particle acceleration. Measurements of solar energetic particles in space, near the first Sun-Earth Lagrange point (L1) onboard the SOHO spacecraft, and in geostationary orbit onboard the GOES-19 spacecraft, are presented, revealing a long-duration, hard-spectrum intense solar particle event. The analysed event produced radiation hazards at high-latitude flight-altitude regions and triggered multiple GLE alarms in the monitoring systems. This work presents a solid, verified basis for a comprehensive, detailed analysis of GLE #77 produced by a strong eruptive event on the Sun.

* Corresponding author.
E-mail address: ilya.usoskin@oulu.fi (I. Usoskin).

https://doi.org/10.1016/j.asr.2026.03.023
0273-1177/

1. Introduction

The Earth's radiation environment, specifically in the troposphere and above, is largely defined by the omnipresent, slightly variable flux of Galactic Cosmic Rays, but may sometimes be greatly affected by sporadic intense events when solar energetic particles (SEPs) are accelerated during solar eruptive events such as flares and coronal mass ejections (CMEs) in the solar atmosphere (e.g., Desai and Giacalone, 2016; Vainio et al., 2009). Such SEP events occur quite often when the Sun is active and are typically detected in outer space, since Earth is protected by both its geomagnetic field and thick atmosphere. However, rarely, SEP events can be very energetic and intense, and initiate nucleonic-muon-electromagnetic cascades in the atmosphere, with secondary particles detected on the ground, mostly by neutron monitors (NMs). These types of SEP events are conventionally called Ground-Level Enhancements (GLEs), which are defined as (Poluianov et al., 2017):

> A GLE event is registered when there are near-time coincident and statistically significant enhancements of the count rates of at least two differently located neutron monitors including at least one neutron monitor near sea level and a corresponding enhancement in the proton flux measured by a space-borne instrument(s).

At present, 77 GLEs have been registered since 1942 – the data are collected at the International GLE Database (IGLED) at https://gle.oulu.fi (Usoskin et al., 2020) – implying an average GLE rate of one event every 1.08 years. However, their occurrence distribution is highly uneven (Shea and Smart, 2000) in time –they tend to occur around the maximum and early declining phases of the solar cycle– and integral intensity (three orders of magnitude – Asvestari et al., 2017). The strongest known GLE of the neutron-monitor era took place on 23-Feb-1956 (GLE #5) and was characterised by the maximum integral intensity of ≈6000 %·hr (Usoskin et al., 2020; Hayakawa et al., 2024). Only five GLEs had the integral intensity above 500 %·hr, viz., less than one per solar cycle (Asvestari et al., 2017). The last strong GLE #69 took place on 20-Jan-2005, viz. 20 years ago, at the declining phase of solar cycle 23.

The previous solar cycle 24 was weak and produced only a couple of moderate GLE events, #71 in May 2012 (Mishev et al., 2014; Battarbee et al., 2018; Perez-Peraza et al., 2020) and #72 in September 2017 (Mishev et al., 2018; Mavromichalaki et al., 2018). Cycle 25 started in 2020 and produced four weak GLEs #73 through #76, with the strongest one being GLE #74 on 11-May-2024 (Papaioannou et al., 2025) with the maximum integral intensity of ≈10 %·hr. However, recently, GLE #77 occurred on 11-Nov-2025 and appeared to be the strongest one, in terms of the integral intensity, over the past 36 years, since GLE #42 on 29-Sep-1989, and the fourth strongest over the neutron-monitor era. The SEP event was recorded by numerous in situ space-borne detectors at different locations in the inner heliosphere closer to the Sun, which makes it one of the best-observed strong SEP events. The event was apparently a complex multi-component event appearing on the variable Galactic Cosmic Ray background, and a full analysis of its characteristics is pending.

The purpose of this paper is to collect, present and discuss available verified data from selected ground-based and space-borne instruments along with the ambient solar and heliospheric conditions. This will form a solid and reliable basis for more detailed studies and physical interpretations of this very interesting and challenging SEP event.

2. Ground level enhancement

GLE #77 was recorded by the worldwide network of neutron monitors and the Mini Neutron Monitor aboard the Polarstern vessel, as summarised here. An example of the time profile, detrended for the changes in the Galactic Cosmic Ray background, of the polar high-altitude SOPO (South Pole) neutron monitor is shown in Fig. 1 upper panel. Two distinct components are clearly seen: a short impulsive phase (approximately 10:10 – 10:50 UT), and a long gradual phase lasting for up to 17 h, until about 04 UT of the next day. The lower panel of Fig. 1 shows the cumulative integral intensity of GLE #77 for the SOPO neutron monitor. The detrending and the integral intensity computations were made following the procedure described in Usoskin et al. (2020): the pre-increase level was set to 08:00–10:00 UT of 11-Nov-2025, and the background, corresponding to the gradual recovery after the Forbush decrease of 08-Nov-2025, was presented by a linear trend fitted between 08–10 UT and 22–24 UT of 11-Nov-2025, as a new Forbush decrease started around 00 UT of 12-Nov-2025. While SOPO neutron monitor recorded a clear two-phase structure, many other detectors observed only one phase (see, e.g., Fig. 13 in appendix A), as summarised in Table 1.

Values of the geomagnetic rigidity cutoff P_c were computed for all stations by the Open-source geomagneToSphere prOpagation tool (OTSO – Larsen et al., 2023), using actual geomagnetic conditions for 10:30 UT on 11-Nov-2025. Cutoff computations were conducted within a realistic model magnetosphere constructed using a superposition of the international geomagnetic reference field (IGRF v.14 – Alken et al., 2021) and the Tsyganenko 2015 model (TA15 – Tsyganenko and Andreeva, 2015). Input parameters for TA15 were obtained from National Oceanic and Atmospheric Administration (NOAA)[1] at the time of the event, and the TA15-required magnetic coupling N-index (Newell et al., 2007) was computed following the formalism outlined in Newell et al. (2007) and Tsyganenko and Andreeva (2015). The detailed

[1] The list of acronyms used throughout the paper is available in C

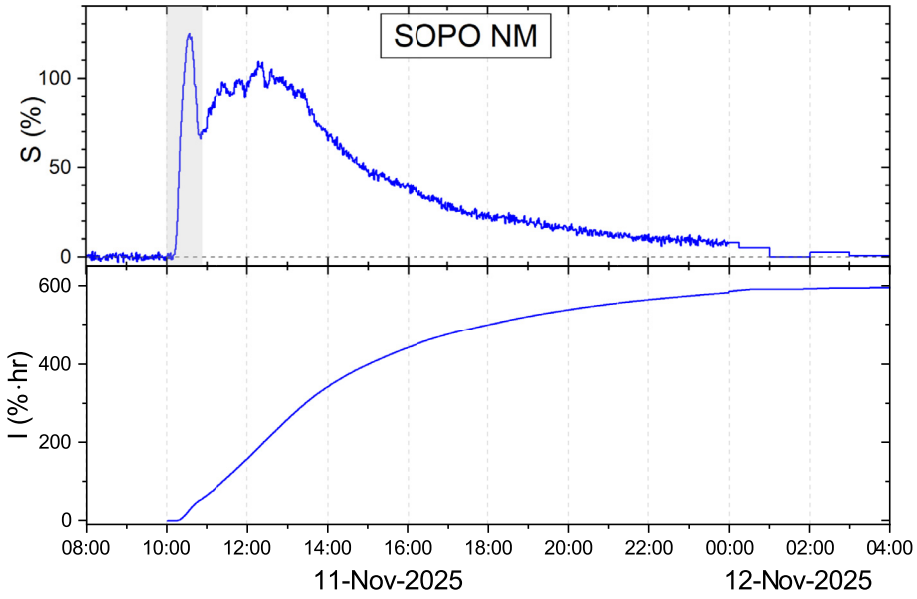

Fig. 1. GLE #77 recorded by the South Pole (SOPO) neutron monitor with 1-min resolution. The relative count rate (in %) and the integral intensity (in %·hr) are depicted in the upper and lower panels, respectively. The percentage is with respect to the Galactic Cosmic Ray background for the pre-increase interval of 08–10 UT of 11-Nov-2025. The count rate was detrended as specified in the text. The grey shaded area represents the first impulsive phase of the event.

computation results and input parameters for these computations are provided in the electronic supplement.

The second, gradual phase was detected by most high- and mid-latitude stations with $P_c < 5$ GV, suggesting that it was nearly isotropic with a relatively soft spectrum. In contrast, the impulsive phase was detected by only about half of the neutron monitors, including those with a high cutoff up to 12 GV (ICRO and HLEA detectors). This implies that the impulsive phase had a hard spectrum, but was highly anisotropic. The highest (15-min smoothed) value, among standard neutron monitors, of the impulsive peak, $A1$, of 125% was recorded at MWSN, closely followed by SOPO (117%). For the bare (lead-free) neutron monitors, $A1$ peaks reached 164% and 155% for MSWB and SOPB, respectively. Interestingly, neutron monitors, whose asymptotic acceptances were directed off the ecliptic, viz., DOMB/DOMC and THUL, didn't observe the impulsive phase, confirming its anisotropic nature. A map (in GSE coordinates) of the neutron monitor peak responses to the impulsive phase of the GLE is shown in Fig. 2. As seen, the detectable responses (blue circles) were concentrated around the apparent interplanetary magnetic field (IMF) direction within roughly 60°, while neutron monitors with a larger angular distance didn't record the impulsive phase. The formal weighted centroid (grey-shaded area) of the blue circles is centred very close to the apparent IMF direction.

The observed notable anisotropy during the event onset implies that neutron monitors with maximal count rate increases responded to SEP fluxes with narrow pitch angles, likely with asymptotic cones close to the direction of the interplanetary magnetic field lines (e.g., Cramp et al., 1997; Bombardieri et al., 2008). This is expected because the recorded GLE intensity is affected by the asymptotic viewing direction and geomagnetic rigidity cutoff at the geographic location of the neutron monitor. Naturally, polar stations with small or no cutoff rigidity record stronger enhancements, because of typically steep rigidity spectra of SEP particles (Vashenyuk et al., 2006; Kocharov et al., 2023). The fast rise of count rates of such neutron monitors as MWSN, NWRK, OULU, PWNK, and SOPO suggests that their viewing directions were close to the particle flux's anisotropy axis, as readily seen in Fig. 2. More details are seen in Fig. 3, which presents asymptotic directions of selected neutron monitors, computed using the OTSO tool (Larsen et al., 2023), for the GLE onset time (10:10 UT, left panel), and the peak of the gradual phase (12 UT, right panel). The asymptotic directions of the mentioned above neutron monitors lie within 30–60° from the IMF to-the-sun direction. On the other hand, asymptotic directions of neutron monitors missing the impulsive phase, e.g., DOMC, JBGO, TERA or THUL, lie far from the interplanetary magnetic field direction. We note that the SEP propagation in the interplanetary space involves effects of magnetic turbulence and scattering, resulting in the actual arrival direction at Earth being different from the local IMF direction measured at the L1 location. Although a realistic modelling of the SEP propagation is beyond the scope of this data-gathering work, it is planned for a forthcoming scientific analysis of the GLE #77, including modelling of the response of the global neutron monitor network, similarly to Cramp et al. (1997); Vashenyuk et al. (2006); Mishev et al. (2024).

Table 1
Neutron monitors (ordered by the geomagnetic rigidity cutoff), which detected GLE #77 worldwide with the datasets available at the moment of the writing of this paper. The columns represent the standard acronyms of the neutron monitors (see NMDB at https:/nmdb.eu); approximate geographical coordinates, and altitude h in meters above sea level, of the neutron monitor location; effective geomagnetic rigidity cutoff P_c at the GLE onset; magnitude of the first (impulsive) and second (gradual) peaks in the 15-min averaged data, $A1$ and $A2$, respectively; integral intensity I of the GLE in %·hr. Percentages of the increases are above the Galactic Cosmic Ray baseline (see text). Data are available at https://gle.oulu.fi.

NM	Coordinates (°)	h(m asl)	P_c(GV)	$A1$(%)	$A2$(%)	I(%·hr)
DOMB	75.1S, 123.3E	3233	0	–	71	550
DOMC	75.1S, 123.3E	3233	0	–	54	409
TERA	66.7S, 140E	32	0	–	25	181
THUL	76.5 N, 68.7 W	26	0	–	20	138
JBGO	74.6S, 164.2E	30	0	–	27	N/A[‡]
MRNY	66.6S, 93.0E	30	0	30	23	159
SOPB	90.0S, 00	2820	0.1	155	143	802
SOPO	90.0S, 00	2820	0.1	117	106	593
INVK	68.4 N, 133.7 W	21	0.1	–	26	160
MWSB	67.6S, 62.9E	30	0.2	164	28	355
MWSN	67.6S, 62.9E	30	0.2	125	20	277[*]
FTSM	60.0 N, 111.9 W	180	0.3	–	38	193
TXBY	71.4 N, 128.5E	0	0.3	–	27	>135[†]
APTY	67.6 N, 33.4E	181	0.5	33	22	165
PWNK	55.0 N, 85.4 W	53	0.6	34	85	275
OULU	65.1 N, 25.5E	15	0.6	65	20	162
KERG	49.4S, 70.3E	33	1.1	–	30	181
CALG	51.1 N, 114.1 W	1123	1.2	37	59	349
YKTS	62.0 N, 129.4E	105	1.3	–	28	158
KIEL2	55.3 N, 10.1E	54	2.2	9.5	17.5	79
MOSC	55.5 N, 37.3E	200	2.2	–	19	92
NVBK	54.5 N, 83.0E	163	2.6	–	19	104
NWRK	39.7 N, 75.8 W	50	2.7	61	–	120
POLA	55.6 N, 8.6E	0	2.4	–	14[1]	–
IRKT	52.5 N, 104E	435	3.0	–	13	53
DRBS	50.1 N, 04.6E	225	3.3	–	11	30
LMSK	49.2 N, 20.2E	2634	3.7	–	11	37
JUN1	46.6 N, 8.0E	3500	4.5	–	7	20
JUNG	46.6 N, 8.0E	3500	4.5	–	7.2	20
BKSN	43.3 N, 42.7E	1700	5.4	3	–	5.1
AATB	43.14 N, 76.6E	3340	5.9	3.4	–	5.3
ROME	41.9 N, 12.7E	0	6.1	2	–	2.2
ROZH	41.7 N, 24.7E	1730	6.4	3	–	2
PTFM	26.7S, 27.1E	1351	7.0	4.7	–	12
CALM	40.5 N, 03.1 W	708	7.0	2	–	<1
MXCO	19.3 N, 260.8E	2274	7.4	4.2	–	4.8
ATHN	38.0 N, 23.8E	260	8.2	3.9	–	2.4
ICRO	28.3 N, 16.5 W	2373	11.5	2	–	<1
HLEA	20.7 N, 156.3 W	3050	12.3	2	–	1

[1] Statistics do not allow us to differentiate the two components, see Fig. 13.
[†] data break after 17:50 UT.
[*] gaps interpolated for the calculation of I.
[‡] cannot be reliably defined because of significant data gaps.

The integral intensity of the GLE shows a clear tendency that lower-cutoff neutron monitors recorded the event at a higher intensity level – the maximum was recorded at SOPO (≈590 %·hr) and DOMC (≈410 %·hr) for standard neutron monitors, and SOPB (≈800 %·hr) and DOMB (≈550 %·hr) for bare (lead-free) neutron monitors, which are sensitive to lower-energy cosmic particles. An increase was also observed (Chilingarian et al., 2025) by a solar neutron telescope in Mt. Aragats ($P_c \approx 6.7$ GV). However, since it is not a standard NM, its percentage increase cannot be directly compared to the data from the NM network.

3. Solar and heliospheric conditions

3.1. Eruptive solar flare

GLE #77 was associated with a strong soft X-ray burst (X 5.1: peak flux in the 0.1–0.8 nm wavelength range 5.1×10^{-4} W m^{-2}) reported by the Space Weather Prediction Center of NOAA (https://solarmonitor.org/?date = 20251111) to start at 09:49 UT with a peak at 10:04 UT. The eruption occurred at N23° W24° in active region NOAA 14274 in the north-western solar quadrant.

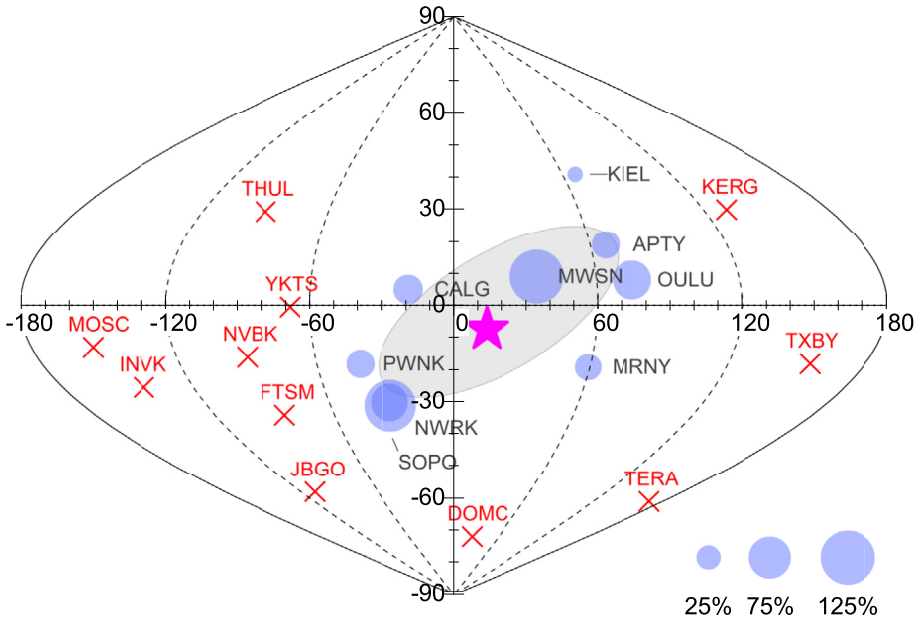

Fig. 2. Map (sinusoidal projection, GSE coordinates) of the worldwide neutron monitor peak responses to the impulsive phase of GLE #77. The coordinates of the points correspond to the asymptotic directions (for the moment of 10:30 UT) of the neutron monitor at the geomagnetic rigidity cutoff P_c or 1 GV if P_c<1 GV. The area of the blue circles represents the peak response in % (see Table 1) as indicated in the bottom panel. Neutron monitors without a detectable impulsive-phase peak are indicated by the red crosses. The magenta star depicts the apparent interplanetary magnetic field sunward direction for the onset of the event. The grey ellipse denotes the weighted centroid of the responses (blue circles), which includes 68% of the responses.

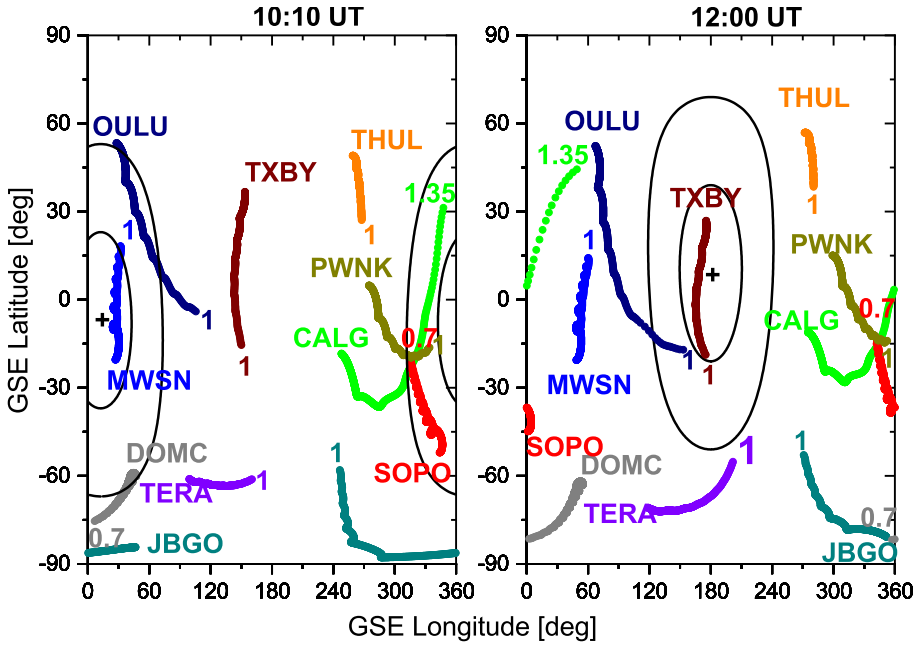

Fig. 3. Computed asymptotic directions for selected neutron monitors during the GLE #77 onset time 10:10 UT on 11-Nov-2025 (left panel) and the maximum of the gradual phase at 12:00 UT (right panel). The standard abbreviations, the corresponding colour lines, and numbers indicate the neutron monitors and their asymptotic directions, plotted in the rigidity range 1–8 GV, respectively. For DOMC and SOPO neutron monitors, the lines are plotted for rigidities 0.7–8 GV. The black cross depicts the IMF direction, corrected for the transit time between the L1 location and Earth according to the measured solar wind speed. The lines of equal pitch angles relative to the IMF direction are plotted for 30° and 60°.

Fig. 4 shows six snapshots during the eruption at 17.1 nm wavelength in the extreme ultraviolet (EUV) range between 09:50 UT and 10:14 UT, as observed by the *Atmospheric Imaging Assembly* (AIA, Lemen et al., 2012) aboard the NASA *Solar Dynamics Observatory* mission (SDO, Pesnell et al., 2012). The images have been selected to highlight the main dynamics of the eruption, but we refer the reader to the associated animation (Supplementary material) for a better understanding of the event.

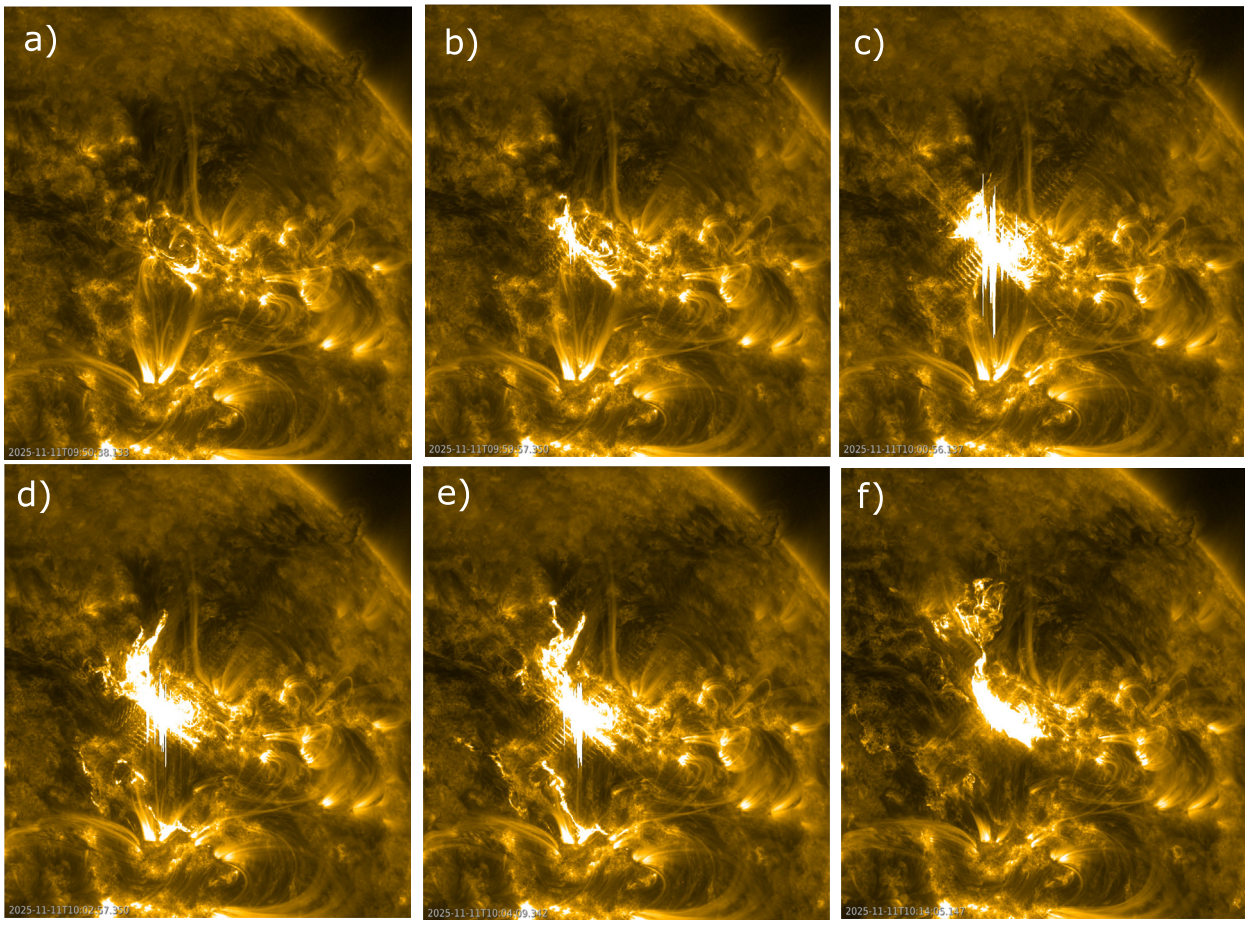

Fig. 4. Evolution of the early phase of the solar eruption occurring in AR 14274. The six panels show images from the AIA instruments onboard SDO at 17.1nm between 09:50 UT and 10:14 UT. Solar north is at the top, west on the right side. The figure presents the main steps of the eruption, showing the precursor (panel a), the main flare phase building up a flux rope through magnetic reconnection (panels b and c) and finally the rise of the flux rope and its interaction with its surroundings (panels d, e and f).

Prior to the eruption, a small filament was observed in the south-western part of the active region. It was associated with the appearance of a first bright compact EUV ribbon nearby starting at 09:50 UT (Fig. 4a), which might be the signature of a precursor to the eruption. Six minutes later, the main phase of the flare started. At 17.1 nm, an elongated flare ribbon was observed since 09:56:41 UT. It elongated, became more intense and had a hook developing at its south-western end (Fig. 4b). This ribbon was located parallel to the inversion line of the magnetic field polarity in the active region. The two J-shaped ribbon geometry was a clear signature of flare reconnection, during which a magnetic flux rope was built up dynamically (Aulanier et al., 2012). In this event, the saturation of the images does not allow us to distinguish the second ribbon on the other side of the polarity inversion line. These flare ribbons are the only EUV structures identified between 09:56 UT and 10:00 UT (Fig. 4c). This strongly indicates that during this time interval, magnetic reconnection was the main driver of the energy release. Starting at 10:02:57 UT, a new EUV structure appeared suddenly north of the flare ribbon (Fig. 4d) and and moved north-eastward away from the active region between 10:02:57 UT and 10:16:57 UT (Fig. 4d, e, f). The shape, impulsivity and overall dynamics of this EUV structure lead us to suggest that this was an erupting flux rope. It is interesting to note that in the meantime, the EUV loops located in the south-east of the active region and connected to it (Fig. 4a) disappeared and new EUV ribbons appeared at their footpoints (Fig. 4d, e). This is a strong indication of magnetic reconfiguration, and we may interpret it as a consequence of magnetic reconnection between the eruptive flux rope and those nearby closed loops. This type of interaction is supported by the observed deflection of some of the EUV loops located on the sides of this loop system. This behaviour is consistent with the fast expansion of a flux rope (Zuccarello et al., 2017). It provided favourable conditions for the development of a shock wave.

The LASCO coronagraph (Brueckner et al., 1995) of the Solar and Heliospheric Observatory (SoHO; ESA/NASA; images consulted at https://soho.nascom.nasa.gov/data/Theater/) observed the first signature of a coronal mass ejection (CME) above the north-western solar limb at 10:24 UT. In the next image at 11 UT, the CME front has pro-

gressed beyond a heliocentric distance of 6 $R_\odot$. It appeared as a faint, nearly circular feature around the solar disk that progressed at a constant speed of 1740 ± 110 km s^{-1} in projection on the sky. From this measurement, we estimated the three-dimensional speed of the front, assuming that the CME can be represented by a hemisphere on top of a cone rooted in the centre of the Sun. This 'cone model' allows for a simple geometric estimate of the speed, as described in Gopalswamy et al. (2010). We used their Eq. (1) and the empirical relationship between the opening angle of the cone and the projected speed of halo CMEs quoted there. On 11-Nov-2025, the heliographic latitude of the disk centre seen from Earth was $B_0 = 3.27°$ (https://bass2000.obspm.fr/ephem.php). With the heliographic coordinates of the flare given above, the three-dimensional speed of the CME front is about 2100 km s^{-1}.

3.2. The heliosphere near Earth

Intense X-ray bursts occurred in AR 14274 before 11-Nov-2025. The Space Weather Prediction Center of NOAA reported X-ray bursts with peaks at 09:19 UT on 10-Nov (X1.2) and at 07:35 UT (X1.7) on 09-Nov. In the coronographic images taken by SOHO/LASCO, a faint CME is first seen above the north-western solar limb at 09:48 UT on 10-Nov. At heliocentric distances above 6 $R_\odot$, a faint halo CME is first seen at 09:54 UT. The statistical relationship between soft X-ray peak fluxes and CME speeds established by Jarry et al. (2023) associates an X1.2 flare with a CME speed of about 1350 km s^{-1}. If it travelled at constant speed, the CME would be expected at 1 AU at about 17 UT on 11-Nov. A later arrival is consistent with the deceleration of the CME during its interplanetary travel (Žic et al., 2015).

A major geomagnetic storm, which started on 12-Nov (Kp = 9- since 0 UT on Nov 12, as reported by the International Service of Geomagnetic Indices https://isgi.unistra.fr/data_plot.php), when count rates of neutron monitors were decaying to their pre-GLE level, was probably caused by the CME launched on 10-Nov. Until that time, the Kp index was below 3 during the GLE. The interplanetary magnetic field near Earth was nonetheless not fully nominal, since in situ measurements (Fig. 8) showed its nearly radial direction (see Fig. 2). Relativistic protons hence arrived when the Earth's magnetosphere was not strongly perturbed, yet they had to travel around the ICME launched on 10-Nov.

3.3. Particle acceleration in the solar atmosphere

Intense radio emission from electrons up to relativistic energies was reported to accompany the flare. The time profile of the early part of the GLE is plotted in Fig. 5 (top panel) together with the time histories of thermal soft X-ray emission in two photon energy ranges (bottom panel). The central panel displays the dynamic radio spectrum between 1 GHz and 1 MHz. This spectral range corresponds to electrons emitting between the low corona and 1–2 $R_\odot$ above the photosphere. The figure combines data from three spectrographs: the ORFEES (Observations Radiospectrographiques pour FEDOME et l'Etude des Eruptions Solaires; Hamini et al., 2021) spectrograph, the Decametric Array (NDA; Lecacheux, 2000) of the Nançay Radio Observatory (France), and the WAVES spectrograph (Bougeret et al., 1995) aboard the *Wind* spacecraft (NASA).

The radio spectrum shows several episodes of electron acceleration in the corona, between 10:01 UT and at least 12 UT on 11-Nov-2025. Since the radio emission with spectral fine structure below 1 GHz is produced by coherent plasma processes, the electron energy was probably of the order of tens of keV. In the following, we focus on the electromagnetic emission around the onset of the GLE and, in particular, its initial anisotropic impulsive peak.

The radio emission started abruptly at 10:01 UT throughout the spectral range 1000–14 MHz. The bursts in the 14–1 MHz range were type III bursts (Nindos et al., 2008; Reid and Ratcliffe, 2014; Klein, 2021) emitted by electron beams that travelled outward through the corona along open magnetic field lines. The earliest onset of the GLE was observed at Newark (NWRK). The rise started at 10:10 UT ±27 s, as inferred from the backward extrapolation of the early rising part of the logarithmic count-rate time profile (see Musset et al., 2023). The cutoff rigidity at the NWRK neutron monitor is 2.7 GV, corresponding to a minimum Lorentz factor $\gamma = 3.0$ and a speed of at least $0.94 \cdot c$ for protons. The delay of 540 s with respect to the start of the type III bursts implies that these protons would have travelled ~2 AU to the Earth if they had been released with the first radio waves. We note that a path length significantly longer than the nominal Parker spiral, such as 2 AU inferred here, is not unusual in SEP events (see, e.g., Fig. 2 in Kahler et al., 2011). The additional length can be explained, for instance, by propagation in a transient magnetic structure such as an ejected magnetic flux rope (Kahler et al., 2011; Wimmer-Schweingruber et al., 2023) or its neighbourhood. In the present work, we consider 2 AU as the maximum distance protons may have travelled to reach the Earth. The minimum distance is the length of the Parker spiral. The solar wind speed at the L1 location (see Fig. 8) was monotonically declining between 21 UT on 10-Nov and 21 UT on 11-Nov. At 10 UT on 11-Nov, it was 440 km s^{-1}. The nominal Parker spiral is rooted at longitude 56°W on a solar wind source surface at 2.5 $R_\odot$ and has a length of 1.14 AU. Taking this length as the minimum estimate of the interplanetary travel path, the protons are expected to arrive at the Earth 1–2 min after the radio waves. With the onset at 10:10 UT, this means that the relativistic protons cannot be released later at the Sun than the radio waves observed at 10:09 UT. The range of possible release times, between 10:01 UT (−500 s) and 10:09 UT (−500 s), corresponds to the first group of radio bursts.

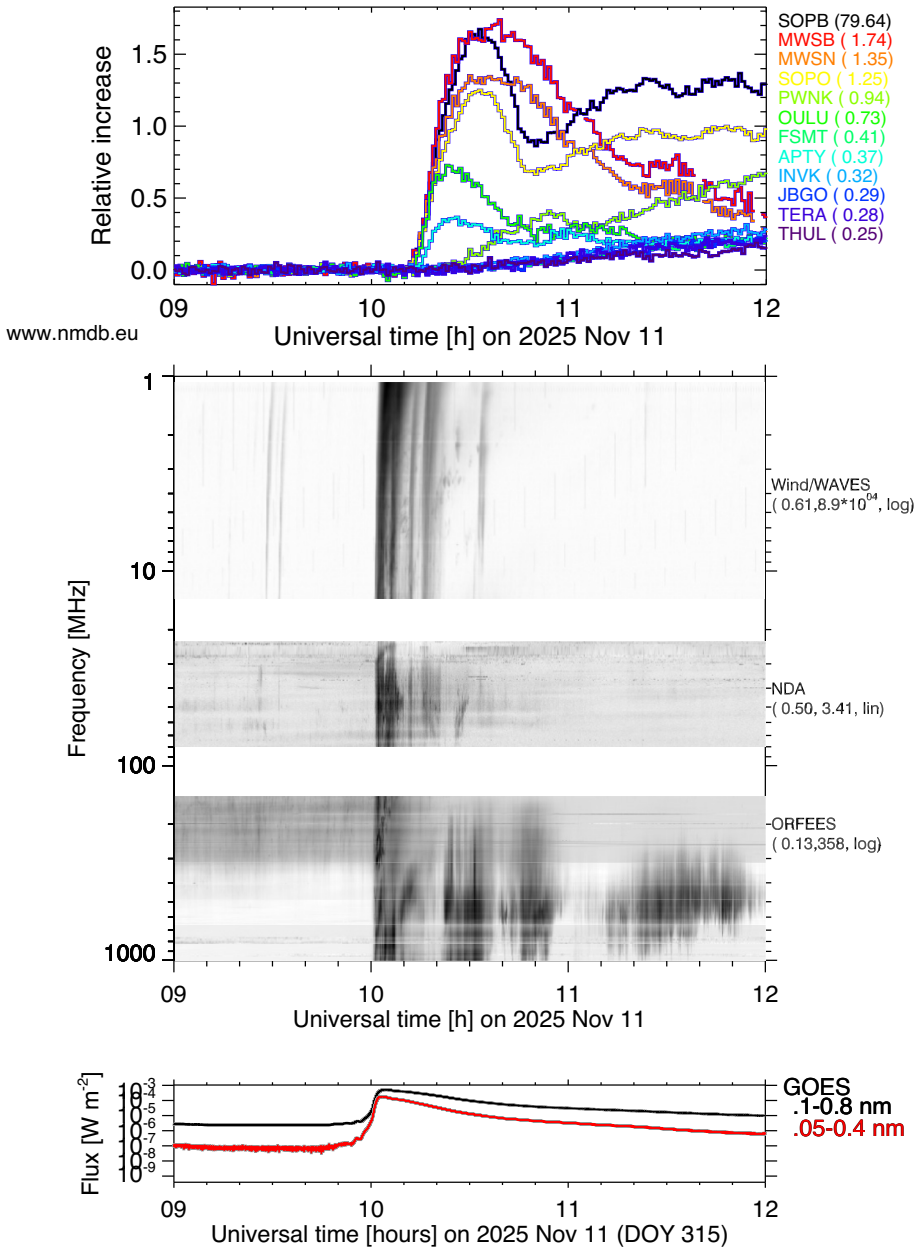

Fig. 5. Time histories of the impulsive part of the GLE as seen by high-latitude neutron monitors (top panel), the time profiles of the soft X-ray burst (bottom panel), and the decimetric-to hectometric radio spectrum. Dark shading shows bright emission.

A closer look at the early hard X-ray, gamma-ray [2] and radio emissions is shown in Fig. 6. The X-ray and gamma-ray time profiles were observed by the Gamma-ray Burst Monitor (GBM;) aboard the Fermi mission (Meegan et al., 2009) until the satellite entered the shadow of the Earth. The radio spectrum is completed by the e-CALLISTO (Benz et al., 2005) station at Siuntio, Finland, in the range 144–100 MHz.

The X-ray (30–70 and 100–300 keV) and gamma-ray (1–10 MeV) light curves show two peaks. The gamma-ray emission comes from relativistic electrons and protons at deka-MeV energies. The first peak of the 30–70 keV and gamma-ray emission occurred at 10:00:53 UT, with the 100–300 keV emission peaking roughly 1 s later. The second peak of the X-ray emission was at 10:01:26 UT (both energy ranges coincide), whereas the gamma-ray emission peaked almost 10 s later, at 10:01:37 UT. A third peak is visible in the X-ray time profile occurring at roughly 10:01:40 UT, which does not appear to be present in the

[2] The emission in the 1–10 MeV range was observed by Fermi Gamma-Ray Burst Monitor (GBM). The Sun was outside of the field of view of the Fermi Large Area Telescope (LAT) at the time of the initial burst, so there is no information on the gamma-ray emission above 30 MeV during this phase. The LAT detected a very significant emission from this flare starting at 11:05 UT. A paper covering the gamma-ray emission from this flare is in preparation.

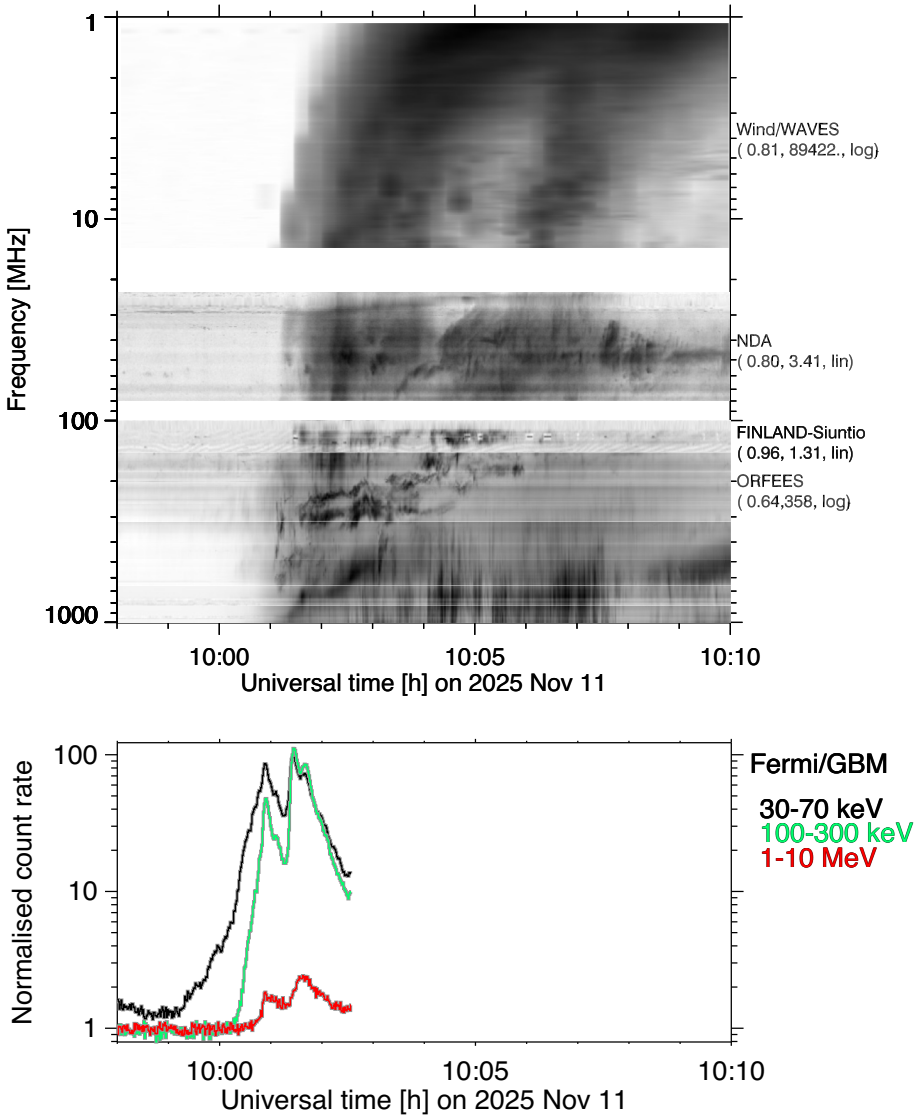

Fig. 6. Dynamic radio spectrum and hard X-ray-gamma-ray emissions during the first group of radio bursts that is associated with the onset of the GLE. The Fermi/GBM observations were interrupted by the satellite entering the shadow of the Earth shortly before 10:03 UT.

gamma-ray data. The first peak of the emission preceded the radio waves below 1 GHz. These observations show that the early acceleration in the corona led to the particle precipitation into the dense chromosphere, and their possible release into low-lying coronal loops, but not to the high corona or into the Heliosphere. The first particle release to the high corona occurred during the second, stronger peak of the hard X-ray and gamma-ray emission.

At frequencies below 14 MHz, the spectrum, acquired with a time resolution of 16 s, shows two type III bursts – the first one between 10:01 and 10:04 UT, and the second at about 10:06–10:07 UT. At higher frequencies (1000–100 MHz), the dynamic spectrum has several components: the long-lasting broadband emission that constitutes a more-or-less uniform background over the entire frequency range is a type IV burst, produced either by electrons with energies of hundreds of keV through gyrosynchrotron emission, or by plasma emission of deka-keV electrons. Numerous bursts in the 1000–300 MHz range are pulsations that are generally understood as modulations of the type IV continuum (Aschwanden, 1987; Aurass et al., 2003; Bouratzis et al., 2015) emitted by trapped non-thermal electrons. On top of the continuum, slowly-drifting bands of emission patches are seen. Their slow drift and rather narrow instantaneous bandwidth show them to be part of a type II burst generated by electrons accelerated at a travelling shock (Mann et al., 2022; Kumari et al., 2023). The gradual penetration of the shock to lower ambient electron densities explains the drift of the emission, generated at the electron plasma frequency and possibly its harmonic.

The first type III burst seen below 14 MHz starts at higher frequencies. It can be tracked in the dynamic spectrogram up to about 200 MHz. At these frequencies, multiple type III bursts can be observed, which merge into a single one at lower frequencies. This is a commonly

observed phenomenon, suggesting that the single type III burst below 14 MHz actually comprises the emission of many electron beams, which follow each other so closely in time that their individual radio spectra merge into a single one when observed with 16-s time resolution below 14 MHz. The observation that these type III bursts started at the drifting band of the type II burst suggests that the electron beams were also accelerated at the shock wave, similar to observations during the GLE #73 of 28-Oct-2021 (Klein et al., 2022). The second type III burst, identified at 10:06 UT at 14 MHz, cannot be tracked to higher frequencies. It points to broadband emission in the 80–25 MHz range, together with bursts that need further analysis. This broadband emission pursued the type II bands seen above 100 MHz, but did not have the spectrum of a type II burst.

The sources of the radio emission could be located at some frequencies by using the Nançay Radioheliograph (NRH, Kerdraon and Delouis, 1997). The source configuration is illustrated at two instants in Fig. 7, where the radio sources at different frequencies are represented by their contours at half maximum, distinguished by different colours from black (444 MHz) over blue to yellow (299 MHz). The contours are plotted on top of EUV images (17.1 nm, AIA), which are represented in inverse greyscale (dark shading indicates bright emission). The left image shows the early phase with the type IV continuum on top of the flaring region. The North-Western source (green and yellow contours) is that of the type II burst. It is located in the direction of the North-Eastward progression of the erupting flux rope observed at 17.1 nm. The radio sources of the type III bursts can, in principle, be located in NRH images at lower frequencies, but they are heavily affected by changes in the refractive index due to density fluctuations in the terrestrial ionosphere. Judging from the association with the type II burst in the dynamic spectrum, the type III burst sources are expected near the type II source, close to the central meridian, at locations which are likely poorly connected to the Earth. The image on the right of Fig. 7 shows again the type IV burst, five minutes later, with a temporary additional source in the north-eastern quadrant near the centre of the solar disk. This source is part of the eruptive event and illustrates its large spatial extent in the corona.

4. Solar energetic particles in space

Fig. 8 shows the evolution of the proton flux at 77–450 MeV measured by Solar and Heliospheric Observatory (SOHO)/ Electron, Proton and Helium Instrument (EPHIN) near the L1 location during GLE #77, and the iron to oxygen ratio measured by SOHO/ Energetic and Relativistic Nuclei and Electron experiment (ERNE) at 50–100 MeV/n, together with IMF and plasma measurements from the Wind spacecraft (also near L1). Despite the gradual nature of the SEP event, the Fe/O ratio was consistently above the nominal coronal value of 0.134, determined from the sample of gradual SEP events (Reames, 1995), indicating the presence of a flare-accelerated SEP component or suprathermal seed particles

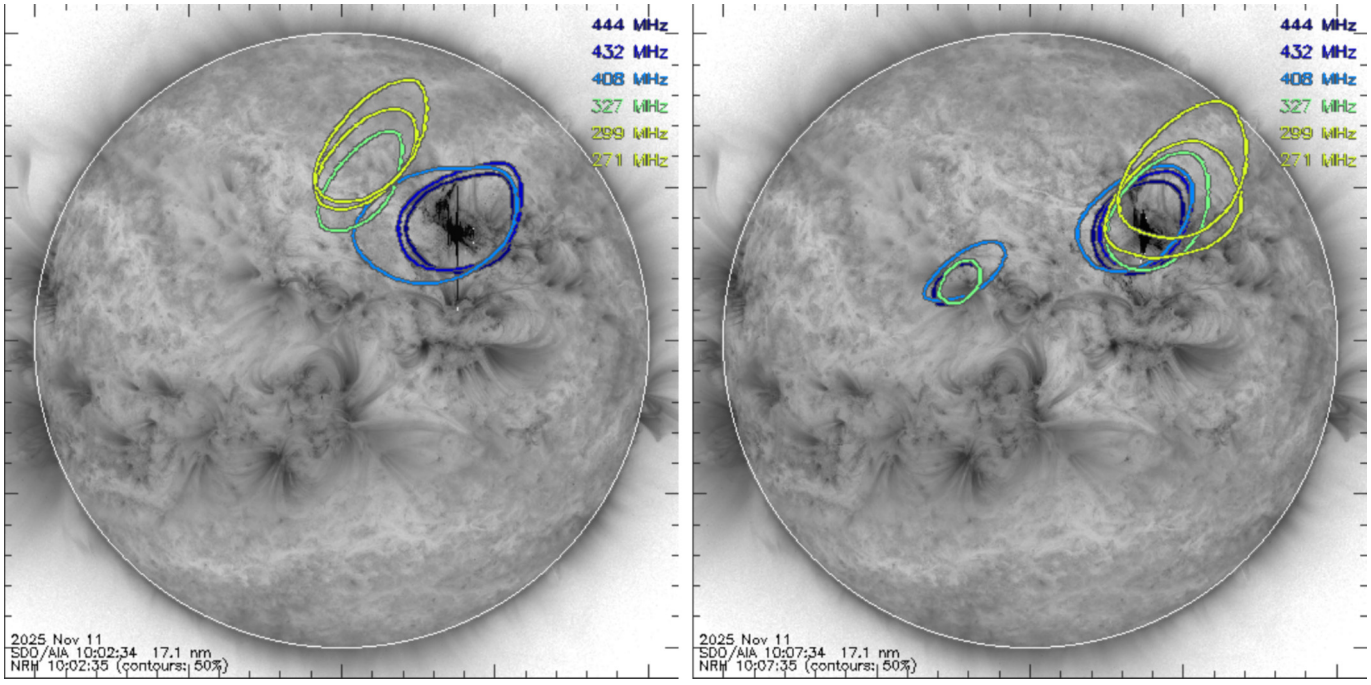

Fig. 7. Two snapshot images during the first 10 min of the eruptive flare on 11-Nov-2025 at 17.1-nm wavelengths (SDO/AIA, inverse grey-scale) with superposed contours at half brightness maximum of radio sources in the 444–299 MHz frequency range (NRH Nançay Radioheliograph). The image on the left shows the type IV burst sources at high frequencies above the flaring region, and the type II burst sources at 217–327 MHz north-eastward of it. The image on the right shows the same type IV burst five minutes later. Solar north is at the top, west on the right side.

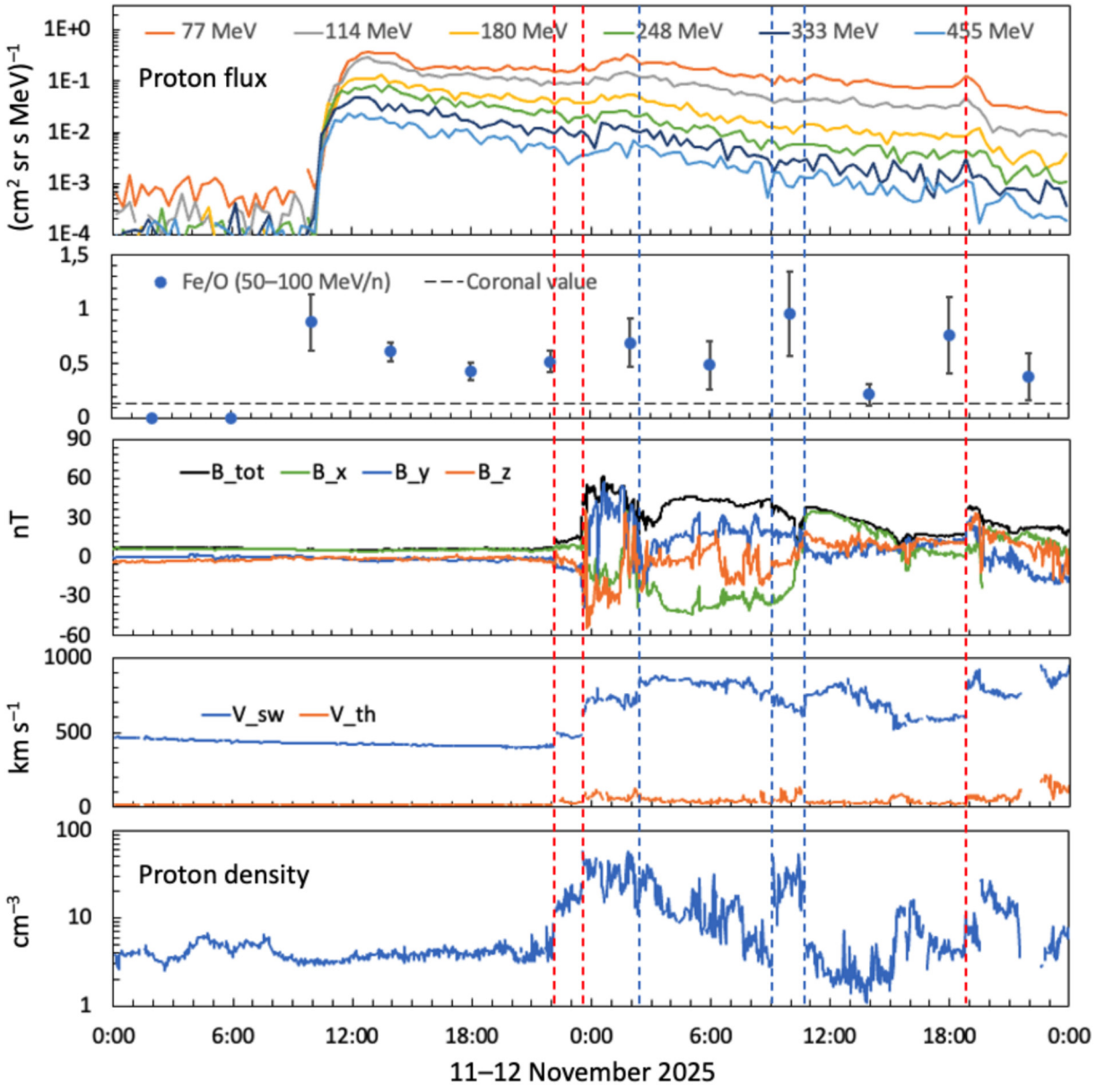

Fig. 8. From top to bottom: Measurements of protons with energies between 77 MeV and 450 MeV from SOHO/ EPHIN (see appendix B); Fe/O ratio (at 50–100 MeV/n) from SOHO/ ERNE; Magnetic field components (GSE coordinates) and strength from Wind/ Magnetic Field Investigation (MFI); and solar wind speed, ion thermal speed, and density from Wind/ Solar Wind Experiment (SWE) (Key Parameter data). The vertical dashed lines depict plasma boundaries, the red ones being (fast-mode) forward shocks and the blue ones other types of boundaries.

with flare origin accelerated at a shock. Panels following the SOHO data are interplanetary magnetic field and solar-wind plasma observations from the *Wind* mission, also near the L1 location.

The vertical dashed lines in Fig. 8 mark boundaries between different plasma domains, as observed in the interplanetary magnetic field and plasma data. The solar wind and interplanetary magnetic field were quiet during the first 12 h of the GLE event. Then, two fast-mode shock waves arrive at L1, closely spaced in time at 22:07 UT and 23:32 UT on 11-Nov-2025, respectively, followed by a turbulent sheath region. Another abrupt increase in the solar wind speed was observed at ~02:20 UT, followed by a region with a bit quieter interplanetary magnetic field, lasting until ~09:07 UT, when the plasma density abruptly increased. Thereafter, the IMF x-component changed sign, and at ~10:45 UT, the density again dropped abruptly. Then, the interplanetary magnetic field experienced a gradual rotation until ~18:50 UT, when another fast-mode shock passed the spacecraft. This shock was likely the one driven by the CME related to the GLE event. The region between the first and the last shocks hosted one or more ICMEs originating from earlier eruptions from the Sun.

Energetic protons were detected in all of the plasma domains observed at L1. The clearest response to the

boundaries was observed at the last shock, where the ~100-MeV proton fluxes peaked. Proton fluxes at all energies started their decay after the last shock passed the spacecraft.

Energetic particles are also measured near Earth by the Geostationary Operational Environmental Satellite (GOES) fleet, each satellite carrying three instruments dedicated to measuring SEP fluxes as part of the Space Environment In Situ Suite (Dichter et al., 2015; Galica et al., 2016): two Solar and Galactic Proton Sensors (SGPS) and an Energetic Heavy Ion Sensor (EHIS). Each SGPS is comprised of three solid-state telescopes covering different energy ranges; one looking westward and the other eastward in the orbit. In general, the westward observations are attenuated less than the eastward observations by the effects of geomagnetic cutoffs, which are evident up to ~80 MeV (Rodriguez et al., 2010; Kress et al., 2013; Kress et al., 2021). During GLE #77, solar energetic particles were observed by GOES-18 and −19 spacecraft. Proton fluxes, observed by the westward-looking GOES-19 SGPS, are shown in Fig. 9. At the onset of GLE #77, the >500 MeV proton flux increased by an order of magnitude over the GCR level. This was the largest increase observed in this channel since the launch of the first SGPS units on GOES-16 in 2016. The largest prior increase in >500 MeV protons, associated with the onset of GLE #72, was only approximately a factor of two over the GCR level (Kress et al., 2021).

EHIS consists of a single solid-state telescope looking radially outward from the Earth in the equatorial plane. It uses the common energy loss vs. residual energy measurement method to bin particles in five energy channels, and a novel Angle Detecting Inclined Sensors (ADIS) system (Connell et al., 2001) to distinguish ions by atomic number, from hydrogen to nickel. The energy range, which is 10–200 MeV for protons, increases with atomic number for the same stopping power in silicon. Carbon (C), nitrogen (N), oxygen (O) and iron (Fe) ion fluxes, observed during this event in the lowest energy channel of GOES-19 EHIS, are shown in Fig. 10. It is noteworthy that the 70 MeV/n Fe fluxes shortly after the onset of GLE #77 have a similar magnitude to those observed after the arrival of the second shock identified in Fig. 8, while the C, N and O fluxes are approximately a factor of two higher after the arrival of this shock.

When comparing the plasma and magnetic field observations by Wind with particle observations near Earth, one should take into account the propagation time of the structures embedded in the solar wind from L1 to Earth. The OMNI dataset provides a time shift based on the solar wind velocity and estimates of the normal direction of the structures. Time shift values in the last two hours of 11 November 2025, i.e., close to the arrival of the first forward shock, are between 36 and 64 min with a mean value of 52 min, and values outside this period have even higher variability. We also calculated the speed of the first forward shock relative to Earth, assuming that it is propagating radially (with a compression ratio of 3.43 and inferred shock speed of 522 km s^{-1}) and determined a time delay of 46 min between Wind and Earth, consistent with the range of values in OMNI data around the shock. However, the comparison of timing between Wind and Earth-based measurements has a lot of uncertainty, so a detailed analysis of all solar wind structures during the event would be needed to provide more accurate timing at Earth. This is beyond the scope of the preliminary analysis of this study.

5. GLE alerts and hazards

Forecasting the high-energy tail of Solar Energetic Particle (SEP) distribution is of great importance for both scientific understanding and practical applications. Particle propagation in interplanetary space depends on their energy: near-relativistic particles associated with GLEs are faster and detected first by the neutron monitors. This provides essential information for estimating the expected

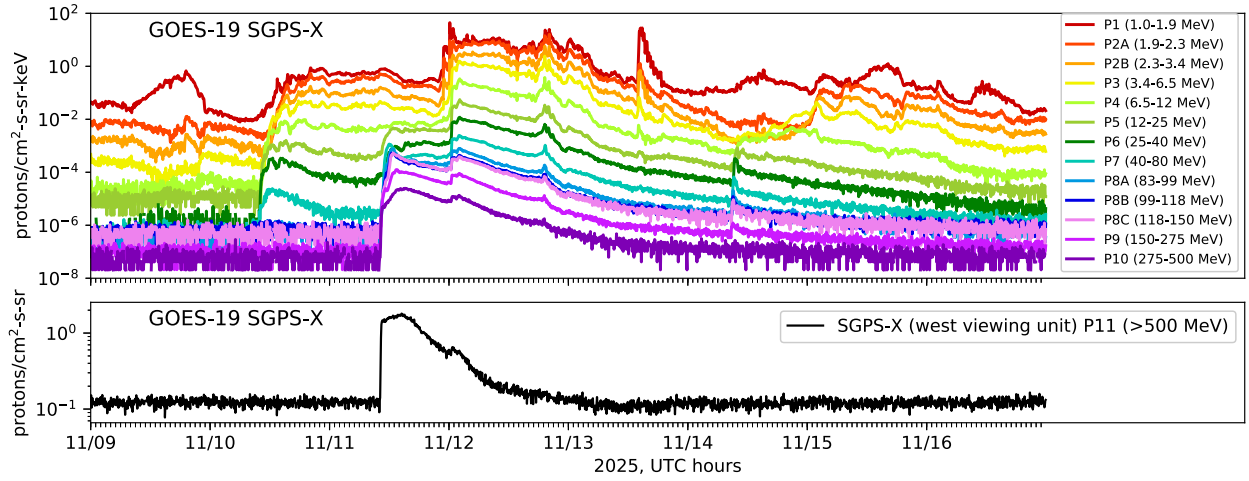

Fig. 9. Proton fluxes (5-min averages) measured by GOES-19/SGPS-X, the west-viewing unit, on 09–15 November 2025. Top panel: differential proton fluxes in 13 channels between 1.0 and 500 MeV. Bottom panel: >500 MeV integral fluxes.

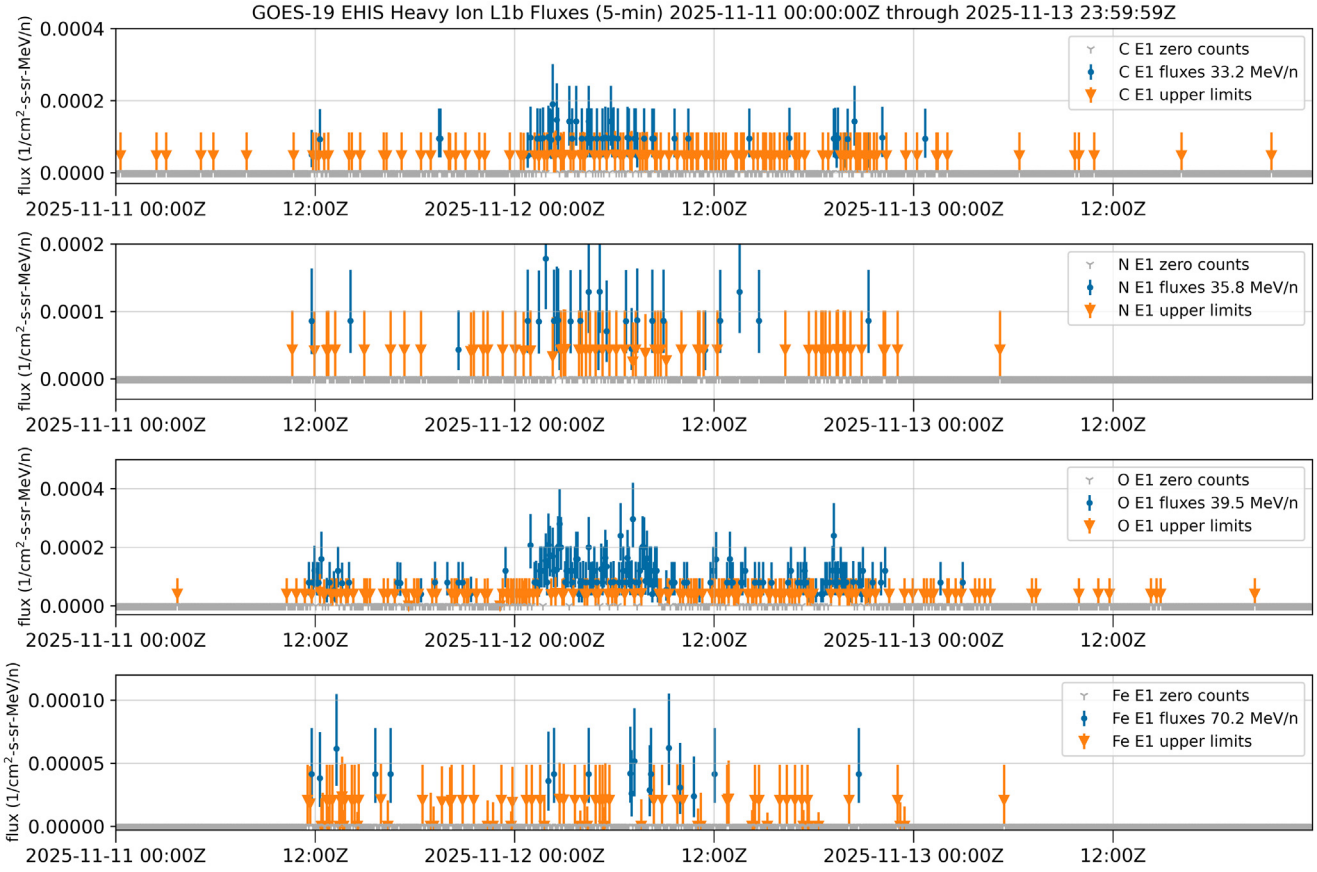

Fig. 10. Heavy ion fluxes (5-min averages) measured by GOES-19/EHIS, 11–13 November 2025, processed in real time. The error bars represent one-sigma random errors. The orange symbols represent upper limits, and the grey symbols indicate zero counts. Panels from top to bottom show: differential carbon fluxes at 33.2 MeV/n; differential nitrogen ion fluxes at 35.8 MeV/n; differential oxygen ion fluxes at 39.5 MeV/n; differential iron ion fluxes at 70.2 MeV/n.

SEP spectrum at lower energies and, more importantly, for assessing potential radiation hazards at flight altitudes due to the anticipated increase in exposure. Consequently, the need for timely notification of GLE events –critical for safeguarding human health and ensuring the reliability of technological infrastructure, including spacecraft design, operations, and avionics– has driven the development of several GLE alert systems (Crosby et al., 2024).

Among the currently existing systems –such as the GLE Alarm developed by the University of Delaware (Kuwabara et al., 2006; Anashin et al., 2009), which uses data from 8 neutron monitors operated by the Bartol Research Institute, and the GLE Alert Signal (currently not available) of the Pushkov Institute of Terrestrial Magnetism, Ionosphere and Radio Wave Propagation of the Russian Academy of Sciences (IZMIRAN), which uses data from 15 neutron monitors – a notable contribution is the GLE Alert system developed by the National and Kapodistrian University of Athens, which has been in continuous operation since 2012 (Mavromichalaki et al., 2024). The latest version of this system, GLE Alert++, incorporates real-time data from a broad network of 27 neutron monitors. Its detection algorithm evaluates count rate variations recorded by the neutron monitor network (NMDB) and operates through two successive stages. At the first stage, a Station Alert is generated by applying the algorithm independently to the 1-min resolution measurements of each station (Mavromichalaki et al., 2024). At the second stage, the system generates a General GLE Alert, commonly referred to simply as the "GLE Alert". This alert is issued based on the number of neutron monitors that enter the Station Alert mode within a predefined 15-min time window. The system defines three escalating levels of alarm. The watch level is activated when three consecutive measurements from a single neutron monitor exceed the threshold, placing that station in Station Alert mode. The warning level follows when two stations simultaneously enter Station Alert mode. Finally, the alert level is reached when at least three stations are in Station Alert mode, at which point the system automatically issues a General GLE Alert and dispatches a notification (Mavromichalaki et al., 2011). The GLE Alert++ system is available through a graphical web interface at European Space Agency (ESA) SWE portal as a federated product under the 'Space Radiation Expert Service Centre', as part of the ESA Space WEather Service NETwork (SWESNET)

project and allows all interested users to receive informational e-mails from the GLE Alert++ system after registering for the service through the ESA website.

On 11-Nov-2025, the neutron monitor network detected GLE #77, prompting the GLE Alert++ system to issue an alert notification to all registered users. Due to the specific characteristics of this event, the system disseminated three successive warning e-mails at 10:14 UT, 11:56 UT, and 12:16 UT. The issuance of multiple alerts can be attributed to the unusually large number of 15 neutron monitors that recorded significant count rate increases, a behaviour that notably distinguishes this event from typical GLE alerts. The first alert was issued by stations SOPB, NEWK and SOPO. The second alert involved contributions from FSMT, PWNK and THUL. Finally, the third alert was issued by SOPB, KERG, PWNK and SOPO.

Fig. 11 shows the general alert status recorded by the GLE Alert++ system software on 11-Nov-2025 at 11:35 UT. The vertical axis refers to the number of stations in alert mode, while the horizontal axis represents time (HH:MM) of the day. The lower panel shows the status of all neutron monitors included in the system (red — alert, orange — warning, gold — watch, green — quiet, blue — delayed and black – offline) as corresponding to 11:35 UT, when FMST, INVK and TERA were in alert mode, PWNK was in warning mode, and IRKT, LMKS and CALM were in watch mode. As seen, the maximum number of stations in alert was 16 (APTY, FSMT, INVK, IRKT, KERG, LMKS, NAIN, NEWK, OULU, PWNK, SOPB, SOPO, TERA, THUL, TXBY, YKTK) at 10:46 UT. The sixteen Neutron Monitor stations that entered Alert mode, distributed across different geomagnetic latitudes, are shown in Fig. 12.

6. Summary

A strong solar particle event, which started on 11-Nov-2025 at around 10:10 UT, had a hard spectrum and a high flux of solar energetic particles, leading to a significant enhancement of the count rates of ground-based neutron monitors. This event was registered as GLE #77, with the peak and integral intensities reaching 125 (165) % and 600 (800) %·hr, respectively, for standard (bare) neutron monitors. This made it one of the strongest GLEs over the past decades. A careful study of the count rate increases of available NM records reveals the presence of SEPs at stations with high rigidity cutoffs, e.g., ICRO and MXCO, which implies a hard spectrum of the GLE-causing solar particles.

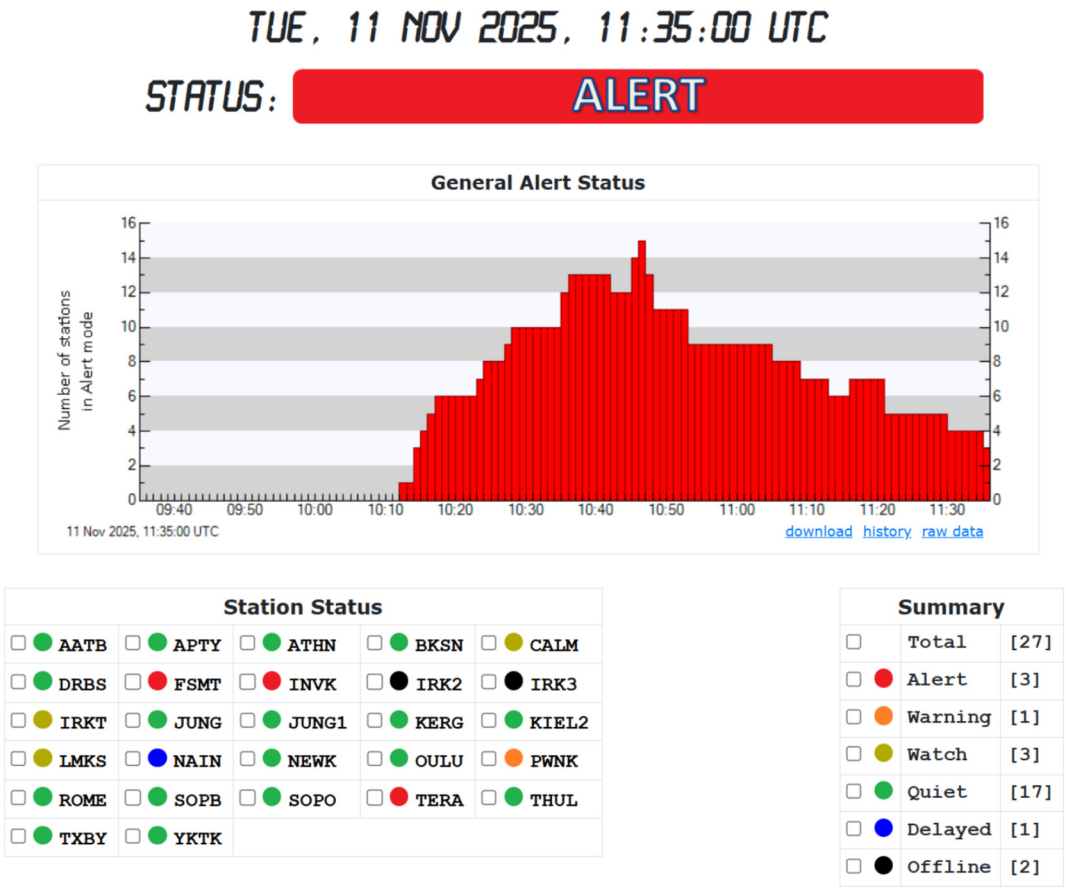

Fig. 11. Evolution of the GLE #77 alert provided by the GLE Alert++ system. `Upper panel`: At 11:35 UT, the GLE Alert++ system was in alert mode, `lower panel`: List of neutron monitors in the Alert++ system with the colour code (see text) – FMST, INVK and TERA (in red) contributed to the alert.

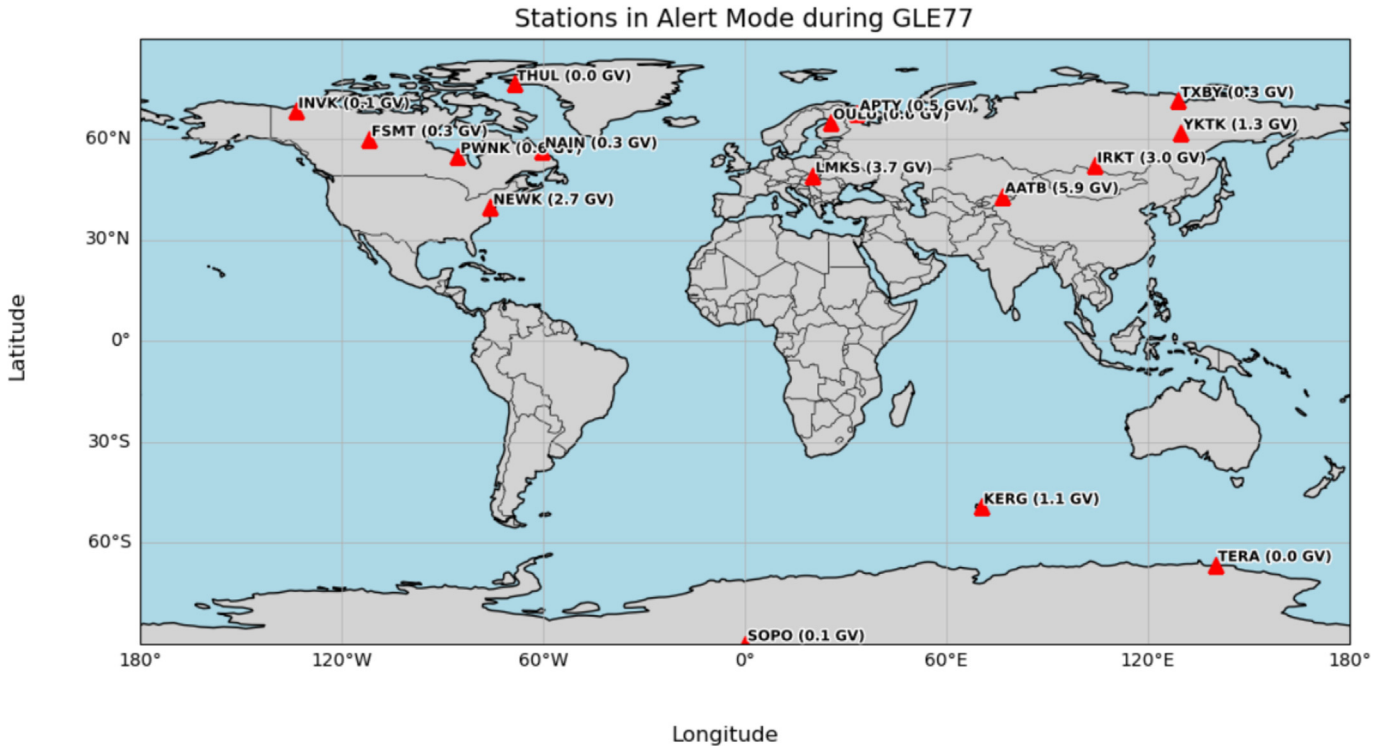

Fig. 12. Stations of the Neutron Monitor network that contributed to Alert mode under the GLE Alert++ system.

The event had a complex structure with two distinct components: a short impulsive phase characterised by a hard energy spectrum and a highly anisotropic flux of energetic particles, and a prolonged gradual phase with a softer spectrum and a broad angular distribution of energetic particles. This corresponds to the two-component structure often observed in other GLEs (e.g. McCracken et al., 2012). The impulsive peak is much clearer in GLE #77 than in most other GLEs, except for 20-Jan-2005 (GLE #69). The event triggered several alerts in the GLE Alert ++ system and may have potentially led to enhanced radiation hazards at flight altitudes and in space. An estimation of the radiation field in the polar region at L350 level (typical flight altitude $\approx$ 10 700 m), based solely on NM count rate increase records (Larsen and Mishev, 2024), that is, without a full reconstruction of SEP spectra, revealed an effective dose of $\approx$ 75 μSv/hr, which is above the threshold for a warning, and close to the alert according to International Civil Aviation Organization (2018) recommendations.

Solar energetic particles were also observed in space, in particular, at the L1 location, by SOHO/EPHIN and SOHO/ERNE detectors, as well as at the geostationary orbit by GOES satellites. The solar particle event lasted for several days and had signatures of transient solar-wind structures. The measured chemical composition, specifically the Fe/O ratio, was indicative of the presence of flare-accelerated particles or suprathermal seed particles with flare origin, accelerated at a shock.

The parent flare on 11-Nov-2025 was eruptive and eventually covered a large solid angle, as manifested by the halo CME observed by SOHO/LASCO with a speed of about 2000 km s^{-1}. The most efficient particle acceleration in the low corona, leading up to relativistic energies, lasted a few minutes only. Electrons attained relativistic velocities very rapidly. Gamma-ray emission had a slightly delayed onset, but a co-temporal maximum with the X-ray peaks. Whether the gamma rays came predominantly from electrons or also included nuclear line emission is unclear for the time being. Non-thermal electron signatures (deka-keV energies) continued over more than an hour, as shown by radio emissions in the middle and high corona. They came from electrons confined in large-scale loops (type IV burst) and from electrons accelerated at a shock wave (type II burst). This shock wave was formed very rapidly during the impulsive flare phase. The radio emission continued for a few minutes, with a source location and timing consistent with the shock being driven by the erupting magnetic flux rope.

The first relativistic nucleons that reach the Earth might have been accelerated within the first ten minutes of the eruptive event. Their anisotropic arrival along the direction of the interplanetary magnetic field suggests a focused transport along the magnetic field. Given their arrival at the Earth 14 h before that of the CME launched on 10-Nov, these nucleons must have travelled around this magnetic structure and hence along an interplanetary path length that was longer than the nominal Parker spiral.

The Earth was not nominally well-connected to the eruptive flare, which was 30° to the east of the footpoint of the Parker spiral connected to Earth. Electrons accelerated at the coronal shock emitted radio waves at a location to the North-East of the flare, hence still farther away from the nominal Parker spiral. To understand the relationship between the relativistic nucleons detected at Earth and the eruptive activity at the Sun, a deeper analysis of the acceleration regions and propagation paths is required.

Declaration of competing interest

The authors declare that they have no known competing financial interests or personal relationships that could have appeared to influence the work reported in this paper.

Acknowledgments

We acknowledge NMDB (http://www.nmdb.eu) and the work of PIs and colleagues from the neutron monitor community, who provided the data used in this paper. Solarwind and IMF data from the Wind mission are available at https://cdaweb.gsfc.nasa.gov/. OMNI data is available at https://omniweb.gsfc.nasa.gov. Data from OULU, DOMB, and DOMC are available at https://cosmicrays.oulu.fi/. SOHO is a project of international collaboration between ESA and NASA. We acknowledge the Italian polar program PNRA (via the AIR-FLOC PNRA OSS-04 project), the French Polar Institute IPEV and the FINNARP for hosting DOMC/DOMB neutron monitors at station Concordia. Radio data were provided by the https://secchirh.obspm.fr and https://rsdb.obs-nancay.fr web sites hosted at Paris Observatory-PSL, by the Wind/WAVES team at Paris Observatory/LIRA, and by the eCALLISTO consortium via https://www.e-callisto.org. EUV images were provided by the teams of the NASA/Solar Dynamics Observatory (SDO) and the Atmospheric Imaging Assembly (AIA), via the Virtual Solar Observatory. KLK acknowledges Q.N. Nguyen and X. Bonnin for efficient help with the Wind/WAVES observations. We acknowledge partial support from the European Union under the ERC Synergy Grant (GA 101166910) and the Horizon Europe Program projects ALBATROS (GA 101077071) and SPEARHEAD (GA 101135044). This work and the ROZH neutron monitor are partially supported by the National Science Fund of Bulgaria under contract KP-06-H64/3. Work in the University of Turku was carried out under the umbrella of the Finnish Center of Excellence in Research of Sustainable Space (Research Council of Finland Grant No. 352847). The Electron, Proton and Helium Instrument (EPHIN) is supported under Grant 50 OC 2302 by the German Bundesministerium für Wirtschaft through the Deutsches Zentrum für Luft- und Raumfahrt (DLR). Work at Paris Observatory was supported by the *Centre National d'Etudes Spatiales* (CNES) and by the *Action Thématique Soleil-Terre* of CNRS. The Haleakala neutron monitor (HLEA) and the associated work at the University of Hawai'i were supported by the U.S. National Science Foundation under award number NSF 2149809. The Kiel team received funding from the European Union's Horizon 2020 research and innovation program under grant agreement No 870405. The team would like to thank the crew of the Polarstern and the AWI for supporting our research campaign. We benefited from the support of the International Space Science Institute (Bern, Switzerland) project No. 585 REASSESS. The GLE Alert++ system forms part of ESA's network of space weather services and service development activities and is supported under ESA Contract 4000134036/21/D/MRP. Work at the University of Colorado was supported by NOAA cooperative agreement NA22OAR4320151. We thank J. J. Connell and C. Lopate for support with the interpretation of the EHIS data. The statements, findings, conclusions, and recommendations are those of the authors and do not necessarily reflect the views of NOAA or the U.S. Department of Commerce.

Appendix A. MNM Installation on the Research Vessel *Polarstern*

A Mini Neutron Monitor (MNM) was installed aboard the German research vessel *Polarstern* to measure variations in Galactic Cosmic Ray (GCR) fluxes under changing geomagnetic and atmospheric conditions. The compact design of the MNM allows operation on mobile platforms while maintaining sufficient counting statistics for scientific studies (Heber et al., 2015).

Since the *Polarstern* regularly travels between polar and equatorial regions, the installation provides unique latitude surveys covering effective vertical geomagnetic cut-off rigidities from below 1 GV to more than 14 GV. This allows detailed investigations of the rigidity dependence of cosmic ray intensities. Atmospheric pressure and temperature effects are corrected using empirically determined coefficients, ensuring consistency with reference neutron monitor stations. Fig. 13 displays the count rate of the MNM during Ground Level Enhancement (GLE) #77, showing a significant flux increase of about 14%. We emphasise that the data presented in Table 1 and stored in the IGLED are detrended to remove the variable background, as described by Usoskin et al. (2020). The statistical significance of the NM count rate increase is considered following the procedure by Poluianov et al. (2025). The baseline level due to GCRs was standardly set as the mean count rate two hours prior to the event onset.

Appendix B. SOHO mission

The NASA/ESA SOHO was launched in 1995 and has been orbiting the Lagrangian point L1 since 1996. The scientific payload of the spacecraft consists of several remote and in situ instruments. The COSTEP Electron, Proton and Helium Instrument (EPHIN, Müller-Mellin et al., 1995) and the ERNE HED are part of

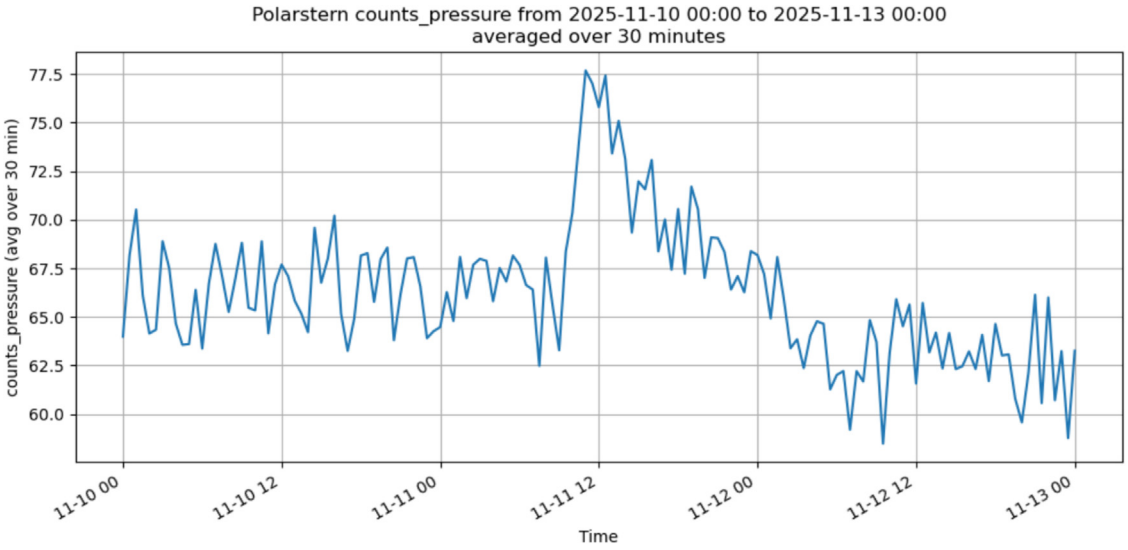

Fig. 13. Measurements by the Polarstern MNM from November 11 to November 12, 2025. Shown is the 30-min pressure-corrected count rate.

the CEPAC suite onboard SOHO. A schematic view of the EPHIN instrument is shown in Fig. 14. The instrument consists of a stack of six Solid State Detectors (SSDs), labelled A–F in Fig. 14, that are surrounded by a scintillation detector (G). Stopping ions are identified by applying the $\frac{dE}{dx} - E$-method. Kühl et al. (2015) utilised the $(\Delta E - \Delta E)$ method to identify the energy range for hydrogen, helium, and electrons that pass through the EPHIN detector stack. Fluxes shown in Fig. 8 were obtained by this methodology.

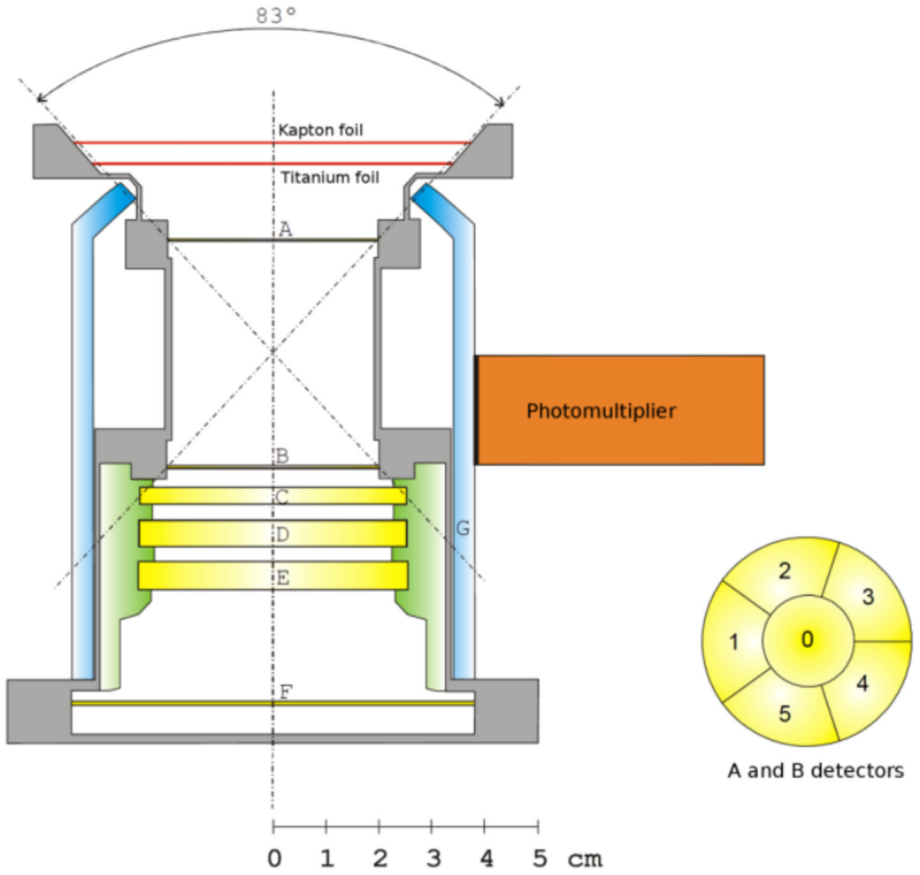

Fig. 14. Sketch of the EPHIN taken from Kühl et al. (2015).

Appendix C. Acronyms

AIA	Advanced Imaging Assembly
AU	Astronomical Unit
ACE	Advanced Composition Explorer
CEPAC	COSTEP – ERNE Particle Analyser Collaboration
CME	Coronal Mass Ejection
COSTEP	Comprehensive Suprathermal and Energetic Particle Analyzer
DOI	Digital Object Identifier
EPHIN	Electron, Proton and Helium Instrument
ERNE	Energetic and Relativistic Nuclei and Electron experiment
ESA	European Space Agency
ESP	Energetic Storm Particle
EUV	Extreme Ultraviolet
FINNARP	Finnish Antarctic Research Program
GBM	Gamma-ray Burst Monitor
GCR	Galactic Cosmic Ray
GEANT	GEometry ANd Tracking
GLE	Ground Level Enhancement
GOES	Geostationary Operational Environmental Satellites
GSE	Geocentric Solar Ecliptic
HED	High Energy Detector
HXR	Hard X-ray
ICME	Interplanetary Coronal Mass Ejection
IMF	Interplanetary Magnetic Field
LED	Low Energy Detector
LET	Low Energy Telescope
MFI	Magnetic Field Investigation
MHD	MagnetoHydroDynamics
NASA	National Aeronautics and Space Administration
MNM	Mini Neutron Monitor
NM	Neutron Monitor
NMDB	Neutron Monitor Data Base
NOAA	National Oceanic and Atmospheric Administration
OTSO	Open-source geomagneToSphere prOpagation tool
SEP	Solar Energetic Particle
SOHO	Solar and Heliospheric Observatory
SOLER	Energetic Solar Eruptions: Data and Analysis Tools
SPEARHEAD	SPEcification, Analysis & Re-calibration of High Energy pArticle Data
SSD	Solid State Detector
STEREO	Solar Terrestrial Relations Observatory
SWA	Solar Wind Analyser
SWE	Solar Wind Experiment

Appendix D. Supplementary material

Supplementary data associated with this article can be found, in the online version, at https://doi.org/10.1016/j.asr.2026.03.023.

References

Alken, P., Thébault, E., Beggan, C.D., Amit, H., Aubert, J., Baerenzung, J., Bondar, T.N., Brown, W.J., Califf, S., Chambodut, A., Chulliat, A., Cox, G.A., Finlay, C.C., Fournier, A., Gillet, N., Grayver, A., Hammer, M.D., Holschneider, M., Huder, L., Hulot, G., Jager, T., Kloss, C., Korte, M., Kuang, W., Kuvshinov, A., Langlais, B., Léger, J.M., Lesur, V., Livermore, P.W., Lowes, F.J., Macmillan, S., Magnes, W., Mandea, M., Marsal, S., Matzka, J., Metman, M.C., Minami, T., Morschhauser, A., Mound, J.E., Nair, M., Nakano, S., Olsen, N., Pavón-Carrasco, F.J., Petrov, V.G., Ropp, G., Rother, M., Sabaka, T. J., Sanchez, S., Saturnino, D., Schnepf, N.R., Shen, X., Stolle, C., Tangborn, A., Tøffner-Clausen, L., Toh, H., Torta, J.M., Varner, J., Vervelidou, F., Vigneron, P., Wardinski, I., Wicht, J., Woods, A., Yang, Y., Zeren, Z., Zhou, B., 2021. International geomagnetic reference field: the thirteenth generation. Earth, Planets and Space 73, 49. https://doi.org/10.1186/s40623-020-01288-x.

Anashin, V., Belov, A., Eroshenko, E., Kryakunova, O., Mavromichalaki, H., Ishutin, I., Sarlanis, C., Souvatzoglou, G., Vashenyuk, E., Yanke, V., 2009. The ALERT signal of ground level enhancements of solar cosmic rays: physics basis, the ways of realization and development. 31st Internat. Cosmic Ray Conf., p. ID:icrc1104.

Aschwanden, M.J., 1987. Theory of radio pulsations in coronal loops. Solar Phys. 111, 113–136. https://doi.org/10.1007/BF00145445.

Asvestari, E., Willamo, T., Gil, A., Usoskin, I., Kovaltsov, G., Mikhailov, V., Mayorov, A., 2017. Analysis of Ground Level Enhancements (GLE): Extreme solar energetic particle events have hard spectra. Adv. Space Res. 60, 781–787. https://doi.org/10.1016/j.asr.2016.08.043.

Aulanier, G., Janvier, M., Schmieder, B., 2012. The standard flare model in three dimensions. I. Strong-to-weak shear transition in post-flare loops. Astron. Astrophys. 543, A110. https://doi.org/10.1051/0004-6361/201219311.

Aurass, H., Klein, K., Zlotnik, E.Y., Zaitsev, V.V., 2003. Solar type IV burst spectral fine structures. I. Observations. Astron. Astrophys. 410, 1001–1010. https://doi.org/10.1051/0004-6361:20031249.

Battarbee, M., Guo, J., Dalla, S., Wimmer-Schweingruber, R., Swalwell, B., Lawrence, D., 2018. Multi-spacecraft observations and transport simulations of solar energetic particles for the May 17th 2012 event. Astron. Astrophys. 612, A116. https://doi.org/10.1051/0004-6361/201731451.

Benz, A.O., Monstein, C., Meyer, H., 2005. Callisto - a new concept for solar radio spectrometers. Solar Phys. 226, 143–151. https://doi.org/10.1007/s11207-005-5688-9, arXiv:astro-ph/0410437.

Bombardieri, D., Duldig, M., Humble, J., Michael, K., 2008. An improved model for relativistic solar proton acceleration applied to the 2005 January 20 and earlier events. Astrophys. J. 682, 1315–1327. https://doi.org/10.1086/589494.

Bougeret, J.L., Kaiser, M.L., Kellogg, P.J., Manning, R., Goetz, K., Monson, S.J., Monge, N., Friel, L., Meetre, C.A., Perche, C., Sitruk, L., Hoang, S., 1995. Waves: the radio and plasma wave investigation on the Wind spacecraft. Space Sci. Rev. 71, 231–263. https://doi.org/10.1007/BF00751331.

Bouratzis, C., Hillaris, A., Alissandrakis, C.E., Preka-Papadema, P., Moussas, X., Caroubalos, C., Tsitsipis, P., Kontogeorgos, A., 2015. Fine structure of metric type IV radio bursts observed with the ARTEMIS-IV radio-spectrograph: association with flares and coronal

mass ejections. Solar Phys. 290, 219–286. https://doi.org/10.1007/s11207-014-0562-2, arXiv:1406.1202.

Brueckner, G.E., Howard, R.A., Koomen, M.J., Korendyke, C.M., Michels, D.J., Moses, J.D., Socker, D.G., Dere, K.P., Lamy, P.L., Llebaria, A., Bout, M.V., Schwenn, R., Simnett, G.M., Bedford, D.K., Eyles, C.J., 1995. The Large Angle Spectroscopic Coronagraph (LASCO). Solar Phys. 162, 357–402. https://doi.org/10.1007/BF00733434.

Chilingarian, A., Sargsyan, B., Kozliner, L., Karapetyan, T., 2025. Solar neutron and muon detection on november 11, 2025: First simultaneous recovery of energy spectra. URL: https://arxiv.org/abs/2512.07859, arXiv:2512.07859.

Connell, J., Lopate, C., McKibben, R., 2001. The angle detecting inclined sensors (ADIS) system: measuring particle angles of incidence without position sensing detectors. Nucl. Instrum. Methods Phys. Res., Sect. A 457, 220–229. https://doi.org/10.1016/S0168-9002(00)00709-9.

Cramp, J., Duldig, M., Flückiger, E., Humble, J., Shea, M., Smart, D., 1997. The October 22, 1989, solar cosmic enhancement: ray an analysis the anisotropy spectral characteristics. Journal of Geophysical Research 102, 24 237–24 248. doi:10.1029/97JA01947.

Crosby, N., Mavromichalaki, H., Malandraki, O., Gerontidou, M., Karavolos, M., Lingri, D., Makrantoni, P., Papailiou, M., Paschalis, P., Tezari, A., 2024. Very high energy solar energetic particle events and ground level enhancement events: forecasting and alerts. Space Weather 22. https://doi.org/10.1029/2023SW003839, e2023SW003839.

Desai, M., Giacalone, J., 2016. Large gradual solar energetic particle events. Liv. Rev. Solar Phys. 13, 3. https://doi.org/10.1007/s41116-016-0002-5.

Dichter, B.K., Galica, G.E., McGarity, J.O., Tsui, S., Golightly, M.J., Lopate, C., Connell, J.J., 2015. Specification, design, and calibration of the space weather suite of instruments on the NOAA GOES-R program spacecraft. IEEE Trans. Nucl. Sci. 62, 2776–2783. https://doi.org/10.1109/TNS.2015.2477997.

Galica, G.E., Dichter, B.K., Tsui, S., Golightly, M.J., Lopate, C., Connell, J.J., 2016. GOES-R space environment in-situ suite: Instruments overview, calibration results, and data processing algorithms, and expected on-orbit performance. In: Earth observing missions and sensors: Development, implementation, and characterization IV, SPIE. pp. 237–251. doi:10.1117/12.2228537.

Gopalswamy, N., Yashiro, S., Michalek, G., Xie, H., Mäkelä, P., Vourlidas, A., Howard, R.A., 2010. A catalog of halo coronal mass ejections from SOHO. Sun and Geosphere 5, 7–16.

Hamini, A., Auxepaules, G., Birée, L., Kenfack, G., Kerdraon, A., Klein, K.L., Lespagnol, P., Masson, S., Coutouly, L., Fabrice, C., Romagnan, R., 2021. ORFEES - a radio spectrograph for the study of solar radio bursts and space weather applications. J. Space Weather Space Clim. 11, 57. https://doi.org/10.1051/swsc/2021039.

Hayakawa, H., Koldobskiy, S., Mishev, A., Poluianov, S., Gil, A., Usoskina, I., Usoskin, I., 2024. Revision of the strongest solar energetic particle event of 23 February 1956 (GLE #5) based on the rediscovered original records. Astron. Astrophys. 684, A46. https://doi.org/10.1051/0004-6361/202348699.

Heber, B., Galsdorf, D., Herbst, K., Gieseler, J., Labrenz, J., Schwerdt, C., Walter, M., Benadé, G., Fuchs, R., Krüger, H., Moraal, H., 2015. Mini neutron monitor measurements at the Neumayer III station and on the German research vessel Polarstern. J. Phys: Conf. Ser. 632, 012057. https://doi.org/10.1088/1742-6596/632/1/012057.

International Civil Aviation Organization, 2018. Manual on Space Weather Information in Support of International Air Navigation. Doc 10100, ICAO, Montreal.

Jarry, M., Rouillard, A.P., Plotnikov, I., Kouloumvakos, A., Warmuth, A., 2023. Parametric study of the kinematic evolution of coronal mass ejection shock waves and their relation to flaring activity. Astron. Astrophys. 672, A127. https://doi.org/10.1051/0004-6361/202245480, arXiv:2303.08663.

Kahler, S.W., Haggerty, D.K., Richardson, I.G., 2011. Magnetic field-line lengths in interplanetary coronal mass ejections inferred from energetic electron events. Astrophys. J. 736, 106. https://doi.org/10.1088/0004-637X/736/2/106.

Kerdraon, A., Delouis, J.M., 1997. The Nançay Radioheliograph. In: Trottet, G. (Ed.), Coronal Physics from Radio and Space Observations. Springer, Berlin, Heidelberg, New York, pp. 192–201.

Klein, K.L., 2021. Radio astronomical tools for the study of solar energetic particles I. Correlations and diagnostics of impulsive acceleration and particle propagation. Front. Astron. Space Sci. 7, 105. https://doi.org/10.3389/fspas.2020.580436.

Klein, K.L., Musset, S., Vilmer, N., Briand, C., Krucker, S., Battaglia, A. F., Dresing, N., Palmroos, C., Gary, D.E., 2022. The relativistic solar particle event on 28 October 2021: Evidence of particle acceleration within and escape from the solar corona. Astron. Astrophys. 663, A173. https://doi.org/10.1051/0004-6361/202243903.

Kocharov, L., Mishev, A., Riihonen, E., Vainio, R., Usoskin, I., 2023. A comparative study of ground level enhancement events of solar energetic particles. Astrophys. J. 958, 122. https://doi.org/10.3847/1538-4357/acfee8.

Kress, B.T., Rodriguez, J.V., Boudouridis, A., Onsager, T.G., Dichter, B. K., Galica, G.E., Tsui, S., 2021. Observations from NOAA's newest solar proton sensor. Space Weather 19. https://doi.org/10.1029/2021SW002750, e2021SW002750.

Kress, B.T., Rodriguez, J.V., Mazur, J.E., Engel, M., 2013. Modeling solar proton access to geostationary spacecraft with geomagnetic cutoffs. Adv. Space Res. 52, 1939–1948. https://doi.org/10.1016/j.asr.2013.08.019.

Kühl, P., Banjac, S., Dresing, N., Goméz-Herrero, R., Heber, B., Klassen, A., Terasa, C., 2015. Proton intensity spectra during the solar energetic particle events of May 17, 2012 and January 6, 2014. Astron. Astrophys. 576, A120. https://doi.org/10.1051/0004-6361/201424874.

Kumari, A., Morosan, D.E., Kilpua, E.K.J., Daei, F., 2023. Type II radio bursts and their association with coronal mass ejections in solar cycles 23 and 24. Astron. Astrophys. 675, A102. https://doi.org/10.1051/0004-6361/202244015, arXiv:2305.18992.

Kuwabara, T., Bieber, J.W., Clem, J., Evenson, P., Pyle, R., Munakata, K., Yasue, S., Kato, C., Akahane, S., Koyama, M., Fujii, Z., Duldig, M.L., Humble, J.E., Silva, M.R., Trivedi, N.B., Gonzalez, W.D., Schuch, N.J., 2006. Real-time cosmic ray monitoring system for space weather. Space Weather 4, S08001. https://doi.org/10.1029/2005SW000204.

Larsen, N., Mishev, A., 2024. Relationship between nm data and radiation dose at aviation altitudes during gle events. Space Weather 22. https://doi.org/10.1029/2024SW003885, e2024SW003885.

Larsen, N., Mishev, A., Usoskin, I., 2023. A new open-source geomagnetosphere propagation tool (OTSO) and its applications. J. Geophys. Res. (Space Phys.) 128. https://doi.org/10.1029/2022JA031061, e2022JA031061.

Lecacheux, A., 2000. The Nançay Decameter Array: A useful step towards giant, new generation radio telescopes for long wavelength radio astronomy. In: Stone, R., Weiler, K., Goldstein, M., Bougeret, J.L. (Eds.), Radio Astronomy at Long Wavelengths. American Geophysical Union, Washington D.C., pp. 321–328. https://doi.org/10.1029/GM119p0321.

Lemen, J.R., Title, A.M., Akin, D.J., Boerner, P.F., Chou, C., Drake, J. F., Duncan, D.W., Edwards, C.G., Friedlaender, F.M., Heyman, G. F., Hurlburt, N.E., Katz, N.L., Kushner, G.D., Levay, M., Lindgren, R.W., Mathur, D.P., McFeaters, E.L., Mitchell, S., Rehse, R.A., Schrijver, C.J., Springer, L.A., Stern, R.A., Tarbell, T.D., Wuelser, J. P., Wolfson, C.J., Yanari, C., Bookbinder, J.A., Cheimets, P.N., Caldwell, D., Deluca, E.E., Gates, R., Golub, L., Park, S., Podgorski, W.A., Bush, R.I., Scherrer, P.H., Gummin, M.A., Smith, P., Auker, G., Jerram, P., Pool, P., Soufli, R., Windt, D.L., Beardsley, S., Clapp, M., Lang, J., Waltham, N., 2012. The Atmospheric Imaging Assembly (AIA) on the Solar Dynamics Observatory (SDO). Solar Phys. 275, 17–40. https://doi.org/10.1007/s11207-011-9776-8.

Mann, G., Vocks, C., Warmuth, A., Magdalenic, J., Bisi, M.M., Carley, E., Dabrowski, B., Gallagher, P., Krankowski, A., Matyjasiak, B., Rotkaehl, H., Zucca, P., 2022. Excitation of Langmuir waves at shocks

and solar type II radio bursts. Astron. Astrophys. 660, A71. https://doi.org/10.1051/0004-6361/202142201.

Mavromichalaki, H., Gerontidou, M., Paschalis, P., Paouris, E., Tezari, A., Sgouropoulos, C., Crosby, N., Dierckxsens, M., 2018. Real-time detection of the ground level enhancement on 10 September 2017 by a. ne.mo.s.: System report. Space Weather 16, 1797–1805. https://doi.org/10.1029/2018SW001992.

Mavromichalaki, H., Papaioannou, A., Plainaki, C., Sarlanis, C., Souvatzoglou, G., Gerontidou, M., Papailiou, M., Eroshenko, E., Belov, A., Yanke, V., Flückiger, E.O., Bütikofer, R., Parisi, M., Storini, M., Klein, K.L., Fuller, N., Steigies, C.T., Rother, O.M., Heber, B., Wimmer-Schweingruber, R.F., Kudela, K., Strharsky, I., Langer, R., Usoskin, I., Ibragimov, A., Chilingaryan, A., Hovsepyan, G., Reymers, A., Yeghikyan, A., Kryakunova, O., Dryn, E., Nikolayevskiy, N., Dorman, L., Pustil'Nik, L., 2011. Applications and usage of the real-time Neutron Monitor Database. Adv. Space Res. 47, 2210–2222. https://doi.org/10.1016/j.asr.2010.02.019.

Mavromichalaki, H., Paschalis, P., Gerontidou, M., Tezari, A., Papailiou, M.C., Lingri, D., Livada, M., Stassinakis, A., Crosby, N., Dierckxsens, M., 2024. An Assessment of the GLE Alert++ Warning System. Atmosphere 15, 345. https://doi.org/10.3390/atmos15030345.

McCracken, K.G., Moraal, H., Shea, M.A., 2012. The high-energy impulsive ground-level enhancement. Astrophys. J. 761, 101. https://doi.org/10.1088/0004-637X/761/2/101.

Meegan, C., Lichti, G., Bhat, P.N., Bissaldi, E., Briggs, M.S., Connaughton, V., Diehl, R., Fishman, G., Greiner, J., Hoover, A.S., van der Horst, A.J., von Kienlin, A., Kippen, R.M., Kouveliotou, C., McBreen, S., Paciesas, W.S., Preece, R., Steinle, H., Wallace, M.S., Wilson, R.B., Wilson-Hodge, C., 2009. The Fermi Gamma-ray Burst Monitor. Astrophys. J. 702, 791–804. https://doi.org/10.1088/0004-637X/702/1/791, arXiv:0908.0450.

Mishev, A., Kocharov, L., Usoskin, I., 2014. Analysis of the ground level enhancement on 17 May 2012 using data from the global neutron monitor network. J. Geophys. Res. 119, 670–679. https://doi.org/10.1002/2013JA019253.

Mishev, A., Koldobskiy, S., Larsen, N., Usoskin, I., 2024. Spectra and anisotropy of solar energetic protons during GLE # 65 on 28 October, 2003 and GLE # 66 on 29 October, 2003. Sol. Phys. 299. https://doi.org/10.1007/s11207-024-02269-z.

Mishev, A., Usoskin, I., Raukunen, O., Paassilta, M., Valtonen, E., Kocharov, L., Vainio, R., 2018. First analysis of GLE 72 event on 10 September 2017: Spectral and anisotropy characteristics. Sol. Phys. 293 (24), 136. https://doi.org/10.1007/s11207-018-1354-x.

Müller-Mellin, R., Kunow, H., Fleißner, V., Pehlke, E., Rode, E., Röschmann, N., Scharmberg, C., Sierks, H., Rusznyak, P., Mckenna-Lawlor, S., Elendt, I., Sequeiros, J., Meziat, D., Sanchez, S., Medina, J., del Peral, L., Witte, M., Marsden, R., Henrion, J., 1995. COSTEP - Comprehensive Suprathermal and Energetic Particle Analyser. Solar Phys. 162, 483–504. https://doi.org/10.1007/BF00733437.

Musset, S., Klein, K.L., Fuller, N., Khreich, G., Wargnier, A., 2023. The time profile of relativistic solar particle events as observed by neutron monitors. J. Space Weather Space Clim. 13, 15. https://doi.org/10.1051/swsc/2023016.

Newell, P.T., Sotirelis, T., Liou, K., Meng, C.I., Rich, F.J., 2007. A nearly universal solar wind-magnetosphere coupling function inferred from 10 magnetospheric state variables. J. Geophys. Res.: Space Phys. 112, A01206. https://doi.org/10.1029/2006JA012015.

Nindos, A., Aurass, H., Klein, K.L., Trottet, G., 2008. Radio emission of flares and coronal mass ejections. Solar Phys. 253, 3–41. https://doi.org/10.1007/s11207-008-9258-9.

Papaioannou, A., Mishev, A., Usoskin, I., Heber, B., Vainio, R., Larsen, N., Jarry, M., Rouillard, A.P., Talebpour Sheshvan, N., Laurenza, M., Dumbović, M., Vasalos, G., Gieseler, J., Koldobskiy, S., Raukunen, O., Palmroos, C., Hörlöck, M., Köberle, M., Wimmer-Schweingruber, R.F., Anastasiadis, A., Kühl, P., Lavasa, E., 2025. The High-Energy Protons of the Ground Level Enhancement (GLE74) Event on 11 May 2024. Solar Phys. 300, 73. https://doi.org/10.1007/s11207-025-02486-0, arXiv:2505.09180.

Perez-Peraza, J.A., Márquez-Adame, J.C., Caballero-Lopez, R.A., Manzano Islas, R.R., 2020. Spectra of the two official gles of solar cycle 24. Adv. Space Res. 65, 663–676. https://doi.org/10.1016/j.asr.2019.10.021.

Pesnell, W.D., Thompson, B.J., Chamberlin, P.C., 2012. The Solar Dynamics Observatory (SDO). Solar Phys. 275, 3–15. https://doi.org/10.1007/s11207-011-9841-3.

Poluianov, S., Mishev, A., Kryakunova, O., Seifullina, B., Nikolayevskiy, N., Usoskin, I., 2025. Ground-level enhancement of 8 June 2024 (GLE 75) caused by solar energetic particles. Solar Phys. 300, 113. https://doi.org/10.1007/s11207-025-02518-9.

Poluianov, S., Usoskin, I., Mishev, A., Shea, M., Smart, D., 2017. GLE and Sub-GLE redefinition in the light of high-altitude polar neutron monitors. Solar Phys. 292, 176. https://doi.org/10.1007/s11207-017-1202-4, arXiv:1711.06161.

Reames, D.V., 1995. Coronal abundances determined from energetic particles. Adv. Space Res. 15, 41–51. https://doi.org/10.1016/0273-1177(94)00018-V.

Reid, H.A., Ratcliffe, H., 2014. A review of solar type III radio bursts. Res. Astron. Astrophys. 14, 773–804. https://doi.org/10.1088/1674-4527/14/7/003.

Rodriguez, J.V., Onsager, T.G., Mazur, J.E., 2010. The east-west effect in solar proton flux measurements in geostationary orbit: A new GOES capability. Geophys. Res. Lett. 37, L07109. https://doi.org/10.1029/2010GL042531.

Shea, M.A., Smart, D.F., 2000. Fifty Years of Cosmic Radiation Data. Space Sci. Rev. 93, 229–262. https://doi.org/10.1023/A:1026500713452.

Tsyganenko, N.A., Andreeva, V.A., 2015. A forecasting model of the magnetosphere driven by an optimal solar wind coupling function. J. Geophys. Res.: Space Phys. 120, 8401–8425. https://doi.org/10.1002/2015JA021641.

Usoskin, I.G., Koldobskiy, S., Kovaltsov, G.A., Gil, A., Usoskina, I., Willamo, T., Ibragimov, A., 2020. Revised GLE database: Fluences of solar energetic particles as measured by the neutron-monitor network since 1956. Astron. Astrophys. 640, A17. https://doi.org/10.1051/0004-6361/202038272.

Usoskin, I.G., Koldobskiy, S.A., Kovaltsov, G.A., Rozanov, E.V., Sukhodolov, T.V., Mishev, A.L., Mironova, I.A., 2020. Revisited Reference Solar Proton Event of 23 February 1956: assessment of the cosmogenic-isotope method sensitivity to extreme solar events. J. Geophys. Res. (Space Phys.) 125, e27921. https://doi.org/10.1029/2020JA027921, arXiv:2005.10597.

Vainio, R., Desorgher, L., Heynderickx, D., Storini, M., Flückiger, E., Horne, R.B., Kovaltsov, G.A., Kudela, K., Laurenza, M., McKenna-Lawlor, S., Rothkaehl, H., Usoskin, I.G., 2009. Dynamics of the Earth's particle radiation environment. Space Sci. Rev. 147, 187–231. https://doi.org/10.1007/s11214-009-9496-7.

Vashenyuk, E., Balabin, Y., Perez-Peraza, J., Gallegos-Cruz, A., Miroshnichenko, L., 2006. Some features of the sources of relativistic particles at the sun in the solar cycles 21–23. Adv. Space Res. 38, 411–417. https://doi.org/10.1016/j.asr.2005.05.012.

Wimmer-Schweingruber, R.F., Berger, L., Kollhoff, A., Kühl, P., Heber, B., Yang, L., Heidrich-Meisner, V., Klassen, A., Gomez-Herrero, R., Rodriguez-Pacheco, J., Ho, G.C., Mason, G.M., Janitzek, N.P., Kouloumvakos, A., Wang, L., Warmuth, A., Lario, D., Carcaboso, F., Owen, C.J., Bučík, R., Pacheco, D., Malandraki, O., Allen, R.C., Rodriguez, L., Shukhobodskaia, D., Espinosa Lara, F., Cernuda, I., Böttcher, S.I., Eldrum, S., Fleth, S., Xu, Z., 2023. Unusually long path length for a nearly scatter-free solar particle event observed by Solar Orbiter at 0.43 au. Astron. Astrophys. 678, A98. https://doi.org/10.1051/0004-6361/202346319.

Žic, T., Vršnak, B., Temmer, M., 2015. Heliospheric propagation of coronal mass ejections: Drag-based model fitting. Astrophys. J. Suppl. 218, 32. https://doi.org/10.1088/0067-0049/218/2/32, arXiv:1506.08582.

Zuccarello, F.P., Aulanier, G., Dudík, J., Démoulin, P., Schmieder, B., Gilchrist, S.A., 2017. Vortex and sink flows in eruptive flares as a model for coronal implosions. Astrophys. J. 837, 115. https://doi.org/10.3847/1538-4357/aa6110, arXiv:1702.00199.